

Autonomous rhythmic activity in glioma networks drives brain tumour growth

David Hausmann^{1,2}, Dirk C. Hoffmann^{1,2,15}, Varun Venkataramani^{1,2,3,15}, Erik Jung^{1,2,15}, Sandra Horschitz^{4,5}, Svenja K. Tetzlaff³, Ammar Jabali^{4,5}, Ling Hai^{1,2,6}, Tobias Kessler^{1,2}, Daniel D. Azorin^{1,2}, Sophie Weil^{1,2}, Alexandros Kourtesakis^{1,2}, Philipp Sievers^{7,8}, Antje Habel^{7,8}, Michael O. Breckwoldt⁹, Matthia A. Karreman^{1,2}, Miriam Ratliff^{2,10}, Julia M. Messmer^{2,11}, Yvonne Yang^{1,2}, Ekin Reyhan^{1,2}, Susann Wendler^{1,2}, Cathrin Löb^{1,2}, Chanté Mayer^{1,2}, Katherine Figarella¹², Matthias Osswald^{1,2}, Gergely Solecki^{1,2,13}, Felix Sahn^{7,8}, Olga Garaschuk¹², Thomas Kuner³, Philipp Koch^{4,5}, Matthias Schlesner^{6,14}, Wolfgang Wick^{1,2} & Frank Winkler^{1,2}✉

Diffuse gliomas, particularly glioblastomas, are incurable brain tumours¹. They are characterized by networks of interconnected brain tumour cells that communicate via Ca²⁺ transients^{2–6}. However, the networks' architecture and communication strategy and how these influence tumour biology remain unknown. Here we describe how glioblastoma cell networks include a small, plastic population of highly active glioblastoma cells that display rhythmic Ca²⁺ oscillations and are particularly connected to others. Their autonomous periodic Ca²⁺ transients preceded Ca²⁺ transients of other network-connected cells, activating the frequency-dependent MAPK and NF-κB pathways. Mathematical network analysis revealed that glioblastoma network topology follows scale-free and small-world properties, with periodic tumour cells frequently located in network hubs. This network design enabled resistance against random damage but was vulnerable to losing its key hubs. Targeting of autonomous rhythmic activity by selective physical ablation of periodic tumour cells or by genetic or pharmacological interference with the potassium channel KCa3.1 (also known as IK1, SK4 or KCNN4) strongly compromised global network communication. This led to a marked reduction of tumour cell viability within the entire network, reduced tumour growth in mice and extended animal survival. The dependency of glioblastoma networks on periodic Ca²⁺ activity generates a vulnerability⁷ that can be exploited for the development of novel therapies, such as with KCa3.1-inhibiting drugs.

Glioblastomas and other incurable gliomas are characterized by high morbidity and mortality due to their invasive growth and notorious resistance against therapies¹. Glioma cells have recently been found to extend ultra-long membrane tube protrusions called tumour microtubes, which connect single tumour cells via gap junctions to functional and communicating multicellular networks^{2–6}. They are found consistently in state-of-the-art animal models of incurable gliomas and human samples^{2–6}. Of note, these tumour cell networks enable multicellular communication by frequent intercellular Ca²⁺ waves^{2–5}, which is partially influenced by neuronal input^{3,4}. In addition, these communicating networks can repair themselves after surgery, leading to local tumour recurrence⁸, and network integration enables tumour cells to better

resist temozolomide chemotherapy and radiotherapy^{2,8}. In light of these findings, we aimed for an in-depth biological and mathematical characterization of the Ca²⁺ communication patterns in those tumour cell networks to better understand their fundamental architecture and function, and to identify potential vulnerabilities.

Ca²⁺ communication in glioma networks

Complex multicellular patterns of Ca²⁺ activity were observed in gliomas originating from xenografted patient-derived human glioblastoma cells in brains of awake mice using *in vivo* multiphoton laser-scanning microscopy^{2,3} (Fig. 1a,b, and Supplementary Video 1, including a second,

¹Neurology Clinic and National Center for Tumor Diseases, University Hospital Heidelberg, Heidelberg, Germany. ²Clinical Cooperation Unit Neurooncology, German Cancer Consortium (DKTK), German Cancer Research Center (DKFZ), Heidelberg, Germany. ³Department of Functional Neuroanatomy, Institute for Anatomy and Cell Biology, Heidelberg University, Heidelberg, Germany. ⁴Central Institute of Mental Health, University of Heidelberg/Medical Faculty Mannheim, Mannheim, Germany. ⁵Hector Institute for Translational Brain Research (HITBR gGmbH), Mannheim, Germany. ⁶Bioinformatics and Omics Data Analytics, German Cancer Research Center (DKFZ), Heidelberg, Germany. ⁷Department of Neuropathology, Institute of Pathology, Ruprecht-Karls University Heidelberg, Heidelberg, Germany. ⁸Clinical Cooperation Unit Neuropathology, German Cancer Consortium (DKTK), German Cancer Research Center (DKFZ), Heidelberg, Germany. ⁹Department of Neuroradiology, Heidelberg University Hospital, University of Heidelberg, Heidelberg, Germany. ¹⁰Neurosurgery Clinic, University Hospital Mannheim, Mannheim, Germany. ¹¹Faculty of Biosciences, Heidelberg University, Heidelberg, Germany. ¹²Institute of Physiology, Department of Neurophysiology, Eberhard Karls University of Tübingen, Tübingen, Germany. ¹³Business Unit Service and Customer Care, Carl Zeiss Microscopy, Jena, Germany. ¹⁴Biomedical Informatics, Data Mining and Data Analytics, Augsburg University, Augsburg, Germany. ¹⁵These authors contributed equally: Dirk C. Hoffmann, Varun Venkataramani, Erik Jung. ✉e-mail: frank.winkler@med.uni-heidelberg.de

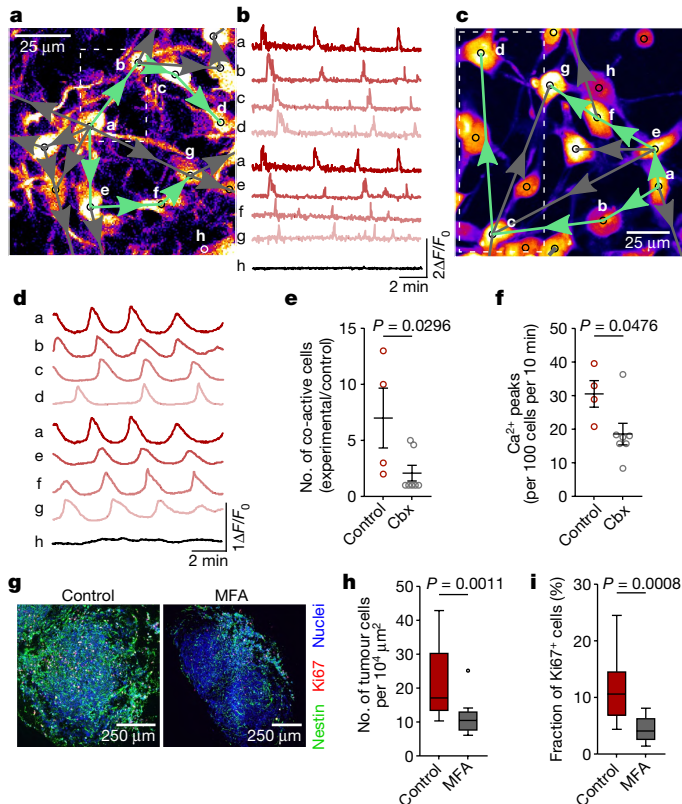


Fig. 1 | Ca^{2+} communication patterns in glioblastoma cell networks. **a**, Network plot of co-active cell pairs derived from Ca^{2+} recordings of S24 tumour cells in vivo; all arrowheads indicate the direction of the transients (green arrowheads indicate the transient sequence depicted in **b**). Dashed outlines in **a** and **c** depict the regions shown in Extended Data Fig. 1a and e. **b**, Synchronized Ca^{2+} transients of tumour microtubule-connected tumour cells. **c, d**, As in **a, b**, but using the novel in vitro tumour cell network growth assay. **e, f**, Intercellular co-activity (**e**) and normalized global Ca^{2+} activity (**f**) in vivo after superfusion of control versus 100 μM carbenoxolone (Cbx, a gap junction inhibitor). $n = 4$ recordings (control) in 3 mice and $n = 7$ recordings (Cbx) in 3 mice. Two-sided t -test. Data are mean \pm s.e.m. **g–i**, Representative immunofluorescence (**g**), tumour cell density (**h**) and fraction of Ki67-positive tumour cells³⁷ (**i**) in tumour-bearing human cerebral organoids derived from the S24 cell line after 14 days of control or 100 μM meclufenamic acid (MFA, a gap junction inhibitor) treatment. $n = 12$ regions in 6 cerebral organoids per group. Two-sided Mann–Whitney test (**h**) and two-sided t -test (**i**).

independent glioma model in Extended Data Fig. 1a–d), and similarly in a newly developed in vitro assay in which glioblastoma cells were grown in a 2D monoculture under stem-like conditions⁹ (Fig. 1c, d, Extended Data Fig. 1e–h, Supplementary Methods and Supplementary Video 1). In all conditions, glioblastoma cells interconnected to multicellular networks and exhibited Ca^{2+} transients travelling between individual tumour cells via their interconnecting tumour microtubes, frequently in recurrent, multicellular patterns (Fig. 1a–d, Extended Data Fig. 1a–m and Supplementary Discussion). Consistently, pharmacological inhibition of gap junctions as well as tumour microtubule formation, but not the inhibition of extracellular transfer of ATP, significantly decreased both intercellular co-activity and global Ca^{2+} activity (Fig. 1e, f and Extended Data Fig. 1n, o). In addition, inhibiting cellular Ca^{2+} entry (Extended Data Fig. 1p–r), Ca^{2+} chelation (Extended Data Fig. 1s–u), and inhibiting tumour cell connectivity via gap junctions in vitro (Extended Data Fig. 1v, w) and in a human cerebral organoid model (Fig. 1g–i and Extended Data Fig. 1x) all strongly reduced the proliferation of glioma cells in a dose-dependent manner, supporting the fundamental biological relevance of both glioma Ca^{2+} activity per se and tumour microtubule-mediated glioma network communication in particular².

Intrinsically rhythmic network activity

Further analyses of Ca^{2+} recordings revealed a small fraction of glioblastoma cells that showed distinct periodic Ca^{2+} oscillations (3.3–4.3% in vivo and 2.6–6.2% in vitro; Fig. 2a, b, Extended Data Fig. 2a and Supplementary Videos 2 and 3). These tumour cells had a particularly large number of tumour microtubule-mediated connections to other cells in the tumour network (Extended Data Fig. 2b–d). Their periodic activity was characterized by a high rhythmicity with low peak-to-peak interval variability (s.d. <15 s; Extended Data Fig. 2e) and a narrow range of Ca^{2+} peak frequencies (mean, 12.5–12.7 mHz in vivo and 9.7–11.3 mHz in vitro) in various experimental conditions (Fig. 2c and Extended Data Fig. 2f). In these experiments, the periodic activity was present in vivo (where tumour cells receive synaptic input from neurons^{3,4}), and similarly and consistently in the in vitro monoculture conditions. This pointed towards a tumour cell-autonomous mechanism, with intrinsic periodic activity possibly triggering Ca^{2+} activity in regionally connected tumour cells. Indeed, inhibiting gap junctions or tumour microtubule formation did not alter the fraction of glioblastoma cells displaying periodic Ca^{2+} activity, but strongly inhibited the majority of non-periodic Ca^{2+} activity of network-connected tumour cells (Fig. 2d, Extended Data Figs. 1o and 2g–i and Supplementary Video 3). Furthermore, glioblastoma cells displaying periodic Ca^{2+} activity (hereafter referred to as ‘periodic cells’) displayed the highest number of Ca^{2+} transients in the tumour cell network, and Ca^{2+} activity declined with increasing degree of separation to these cells (Fig. 2e and Extended Data Fig. 2j). Stochastic measures to estimate the directionality of the intercellular Ca^{2+} waves confirmed that periodic cells were triggering Ca^{2+} signals in other cells in vitro and in vivo (Fig. 2f and Extended Data Fig. 2k). The identity of periodic cells in growing brain tumour networks was found to be plastic, and even adaptive: it partially changed over the time course of 7 days (Fig. 2g, h); ATP was able to specifically increase the number of tumour cells displaying periodic activity (Extended Data Fig. 2m); and new periodic cells appeared after laser ablation of previous cells (Extended Data Fig. 2o, p). Together these findings demonstrate that the rhythmic Ca^{2+} activity in glioblastoma cell networks is a tumour cell-autonomous functional state embodied by a low fraction of glioblastoma cells that influences overall network Ca^{2+} activity in a seemingly hierarchical manner, with considerable plasticity over time.

Architecture of tumour cell networks

To better understand the patterns of intercellular Ca^{2+} communication in glioma, we applied different graph theoretical concepts^{7,10–12} and discovered that functional tumour cell networks have scale-free (Fig. 3a and Extended Data Fig. 3a–d) and small-world (Extended Data Fig. 3e–h) properties, both in vitro and in vivo. Networks with small-world characteristics are known to facilitate quick and efficient communication¹⁰, whereas scale-free networks are characterized by the presence of highly connected hubs^{7,11}. Around 5% of the cells in the network had a number of connections that would rarely or never be observed in a random (Erdős–Rényi) network of comparable size (Fig. 3a and Extended Data Fig. 3a–c), and thus the 5% most functionally connected of all cells were defined as functional network hubs for further analyses⁷ (Fig. 3a–c and Extended Data Fig. 3a–c, i–n). Of note, cells acting as network hubs in these analyses often displayed periodic Ca^{2+} activity (46–48% in vitro and 28–32% in vivo), which occurred only rarely in the numerous non-hub tumour cells (Fig. 3c–e, Extended Data Figs. 3l–q and 4a, b). This network position enables periodic cells to communicate their Ca^{2+} activity efficiently to many other network members^{7,10}.

Resistance and vulnerability of networks

Scale-free networks are highly robust against random damage, and targeted attacks affecting the network hubs leads to a rapid increase

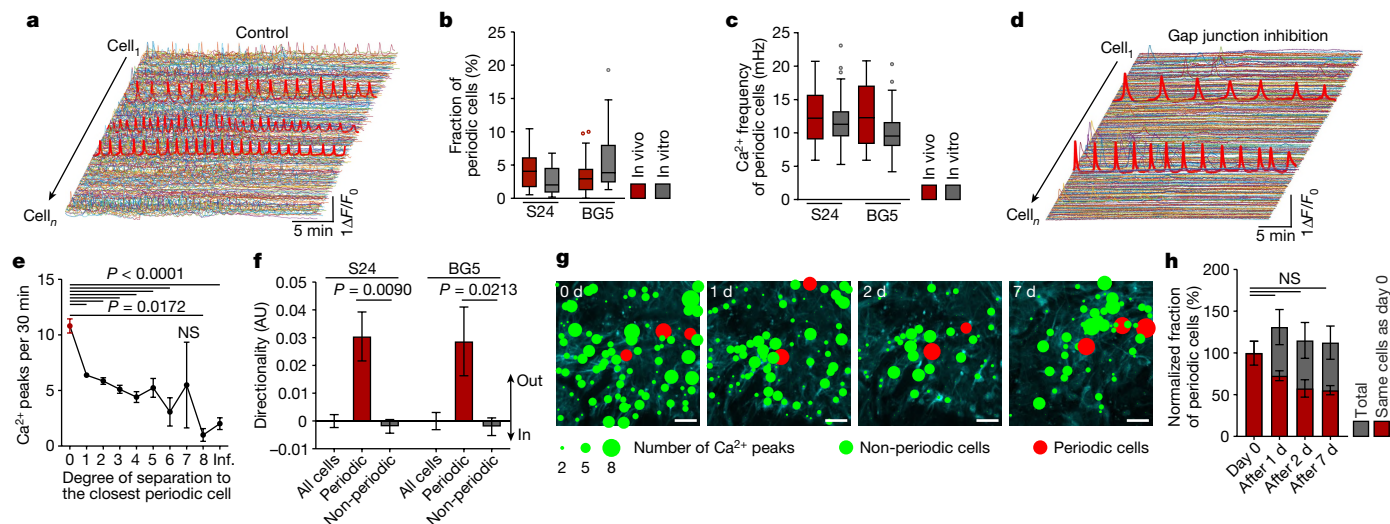


Fig. 2 | A plastic population of cells with periodic Ca^{2+} activity drives network activity. **a, d**, Ca^{2+} traces from a representative recording in vitro using the S24 cell line. Control (**a**) and gap junction inhibition with 100 μM MFA (**d**). Thick red lines are traces of periodic cells. **b**, The fraction of periodic cells among all cells. $n = 24$ recordings from 3 mice (S24 in vivo), $n = 22$ recordings from 9 biologically independent experiments (S24 in vitro), $n = 40$ recordings from 4 mice (BG5 in vivo), and $n = 10$ recordings from 5 biologically independent experiments (BG5 in vitro). **c**, The mean frequency of Ca^{2+} oscillations of periodic cells in vivo and in vitro. $n = 213$ periodic cells (S24 in vivo), $n = 348$ periodic cells (S24 in vitro), $n = 195$ periodic cells (BG5 in vivo), and $n = 324$ periodic cells (BG5 in vitro) from the recordings in **b**. **e**, The number of Ca^{2+} peaks in all cells as a function of the degree of separation d (the number of anatomical cell-cell connections) to the closest periodic cell, using the S24 cell line in vitro. $d = 0$ is shown in red. $n = 120$ cells ($d = 0$), $n = 663$ cells ($d = 1$), $n = 384$ cells ($d = 2$), $n = 203$ cells ($d = 3$), $n = 115$ cells ($d = 4$), $n = 44$ cells ($d = 5$), $n = 13$ cells ($d = 6$), $n = 4$ cells

($d = 7$), $n = 3$ cells ($d = 8$), $n = 53$ cells ($d = \text{infinity}$ (inf.)), which means not connected) from 4 recordings from 4 independent experiments. Kruskal-Wallis test, Dunn's test comparing each group with the periodic cells. **f**, Directionality of the Ca^{2+} signals between communicating periodic and non-periodic cells in vivo. $n = 441$ periodic cells and $n = 4,137$ non-periodic cells from 24 recording from 3 mice (S24 cells) and $n = 167$ periodic cells and $n = 2,363$ non-periodic cells from 40 recording from 4 mice (BG5 cells). Kruskal-Wallis test, Dunn's test. AU, arbitrary units. **g**, Activity plot of representative recordings from the same region in vivo over time using the S24 cell line. Scale bars, 50 μm . **h**, The fraction of periodic cells from identical regions in vivo over time normalized to the number of cells on day 0 of each region. $n = 19$ regions on day 0, $n = 19$ regions on day 1, $n = 8$ regions on day 2, and $n = 6$ regions on day 7 in 4 mice. Kruskal-Wallis test, Dunn's test. Data are mean \pm s.e.m. NS, not significant ($P \geq 0.05$).

of the network diameter and fragmentation of the network⁷. Consistently, the removal of periodic cells (that frequently act as functional network hubs) profoundly compromised the integrity of functional glioblastoma cell networks in silico, whereas random removal of the same number of cells left the networks largely intact (Fig. 3f). To confirm this concept experimentally, we used single-cell-specific laser ablation to remove either all periodic cells or the same number of randomly selected cells from the field of view (Extended Data Fig. 4c,d). Indeed, only the ablation of periodic glioblastoma cells reduced Ca^{2+} activity and size of the functional networks in Ca^{2+} recordings, whereas the ablation of randomly selected cells did not affect the activity or size of the functional networks (Fig. 3g and Extended Data Fig. 4e-g). Consistently, only the ablation of periodic cells, but not of randomly selected cells, led to increased cell death of other network-connected glioblastoma cells (Fig. 3h,i and Extended Data Fig. 4h), indicating their particular importance for tumour network integrity and its related biological functions.

KCa3.1 drives rhythmic activity

To test whether the intrinsic rhythmicity of periodic cells can be molecularly defined and pharmaceutically targeted, we conducted an in vitro screen in the monoculture assay with 17 inhibitors and agonists of molecular mechanisms potentially relevant for Ca^{2+} oscillations¹³. Notably, from all candidates only TRAM-34 and senicapoc, the two inhibitors of the calcium-activated potassium channel KCa3.1, were able to specifically reduce both the prevalence and the Ca^{2+} frequency of periodic cells (Fig. 4a, Extended Data Fig. 2l-n and Supplementary Discussion). Consistently, TRAM-34 sensitive currents characteristic of a KCa3.1 conductance¹⁴ could be detected in a subpopulation (27%)

of morphologically particularly network-connected glioblastoma cells (Fig. 4b). KCa3.1 had previously been associated with glioma cell motility¹⁵⁻¹⁷, sensitization to temozolomide¹⁸ and poorer patient outcome^{16,19}. Inhibiting periodic Ca^{2+} activity with TRAM-34 and senicapoc reduced both global Ca^{2+} activity and tumour cell proliferation in vitro (Extended Data Figs. 2l and 5a,b), and in primary glioblastoma cells growing in human cerebral organoids, without exerting any overt neurotoxic effects (Extended Data Fig. 5c-i). This was further validated by genetic knockout and knockdowns of KCa3.1 using CRISPR and short hairpin RNA (shRNA), respectively, all of which reduced the prevalence of periodic activity and thereby global Ca^{2+} activity, proliferation rate and viability of glioblastoma networks (Extended Data Fig. 6a-g). Owing to the plastic nature of periodic cell identity, it was necessary to manipulate all tumour cells to target periodic activity. However, pharmacological inhibition and genetic knockout of KCa3.1 did not hinder sporadic non-periodic Ca^{2+} activity (Extended Data Fig. 7a-d) and cell-to-cell communication as such (Extended Data Fig. 7e-h). Both also did not affect tumour cell proliferation in in vitro growth conditions that lack network formation and intrinsically rhythmic activity (Extended Data Fig. 7i-q).

Finally, the suppressive effects of the genetic knockout of KCa3.1 on Ca^{2+} activity and proliferation could be rescued by co-culturing KCa3.1-knockout cells with a small fraction (10% or 5%, but not less) of KCa3.1-proficient wild-type cells (Extended Data Fig. 7r-y and Supplementary Video 4). Whereas the KCa3.1KO cells continued to display a negligible number of periodic cells under mixing conditions, the fraction of periodic cells increased substantially in the co-cultured wild-type cells, which led to a reconstitution of the overall fraction of periodic cells (Fig. 4c,d and Extended Data Fig. 7s-u). Consequently, the mixing conditions restored both global (Fig. 4e) and KCa3.1-knockout

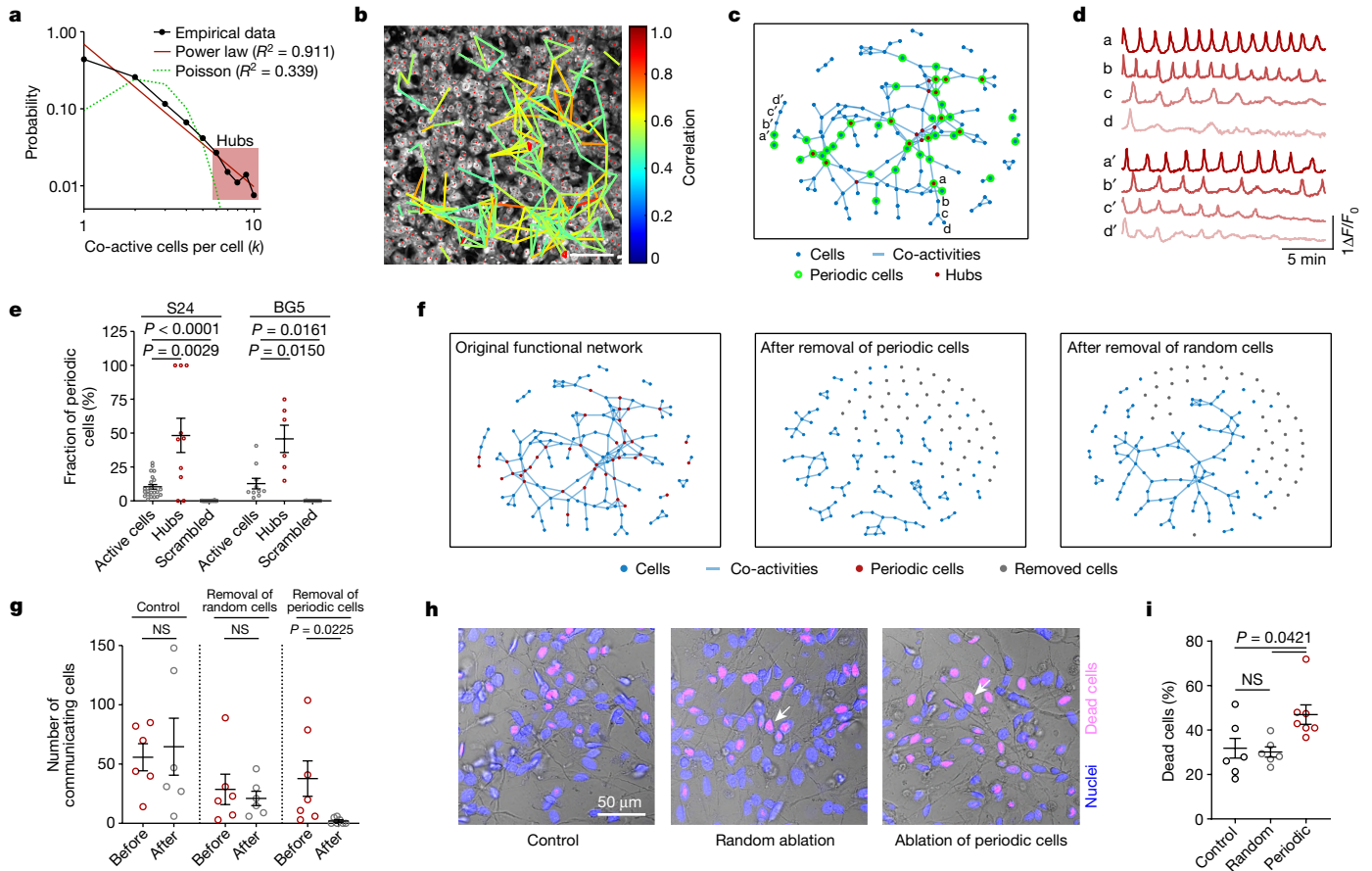


Fig. 3 | Periodic activity in network hubs governs network functionality and resilience. **a**, The mean probability distribution of co-active cells per cell from Ca^{2+} imaging plotted on a log–log scale with linear regression fit (red) and fitted random Poisson distribution (green). BG5 line in vitro. $n = 10$ recordings from 5 biologically independent experiments. **b, c**, Network plot (**b**) and network architecture (**c**) of cross-correlation coefficients larger than cut-off derived from the same Ca^{2+} recording of tumour cells. S24 line in vitro. Scale bar, 100 μm . **d**, Ca^{2+} transients of the tumour microtube-connected tumour cells indicated in **c**. Dark red transients (top lines) originated from a periodic cell. **e**, The fraction of periodic cells among all active cells, all network hubs in experimental data and all cells in scrambled data (randomly shuffled peaks in each trace). $n = 22$ recordings from 9 biologically independent experiments (S24 in vitro) and $n = 10$ recordings from 5 biologically independent experiments (BG5 in vitro). Mixed-effects analysis, Dunnett's test. **f**, Schematic

network plot of the functional glioma network derived from the Ca^{2+} recording in **b, c**, before and after theoretical modelling of removal either of all periodic cells or of the same number of randomly chosen cells within in the network. **g**, The number of communicating cells per field of view in Ca^{2+} recordings in vitro before and 1 h after laser ablation of either no cells (control), all periodic cells, or the corresponding number of randomly chosen active cells. Differences between the conditions before ablation were not significant. Kruskal–Wallis test, Dunn's test. **h, i**, Representative regions (**h**) and fraction of dead (propidium-iodide-positive) tumour cells (**i**) 24 h after laser ablation of either periodic cells (periodic), the corresponding number of randomly chosen active cells (random), or no cells (control). Arrows indicate ablated cells. Kruskal–Wallis test, Dunn's test. **g–i**, BG5 cell line; $n = 6$ recordings (control and random ablation) and $n = 7$ recordings (ablation of periodic cells) in 2 biologically independent experiments. Data are mean \pm s.e.m.

cell-specific Ca^{2+} activity (Fig. 4f and Extended Data Fig. 7v), as well as the respective tumour cell proliferation rates (Fig. 4g–i and Extended Data Fig. 7w–y). The mixing condition also rendered KCa3.1 -knockout cells sensitive towards KCa3.1 inhibition, to which they were resistant in monoculture (Fig. 4h, i and Extended Data Fig. 7w). Together these data support the specific relevance of the KCa3.1 channel for periodic Ca^{2+} activity and demonstrate its growth-stimulating effects, while providing further evidence that the loss of periodic cells is compensated in a plastic manner by the tumour networks.

In addition, genetic overexpression of KCa3.1 , validated with whole-cell patch-clamp electrophysiology, increased the fraction of intrinsically rhythmic cells and Ca^{2+} frequency of their oscillations as well as global Ca^{2+} activity, proliferation rate and cell viability (Fig. 4j and Extended Data Fig. 8a, b), again demonstrating the tight link between KCa3.1 expression, periodic activity and its growth-promoting downstream effects in glioblastoma cells.

In line with these results, periodic cells showed a higher expression of KCa3.1 than the other tumour cells in vitro (Extended Data Fig. 8c, d),

and the small fraction of $\text{KCa3.1}^{\text{high}}$ tumour cells with detectable KCa3.1 expression in vivo (2.6–3.9%; Fig. 4k and Extended Data Fig. 8e) had significantly more tumour microtubes than $\text{KCa3.1}^{\text{low}}$ tumour cells (Fig. 4l and Extended Data Fig. 8f), indicating their strong network integration. Finally, network cells located close to $\text{KCa3.1}^{\text{high}}$ cells had a significantly higher proliferation rate—which could be inhibited by Ca^{2+} chelation—than more distant glioblastoma cells (Extended Data Fig. 8g–k), further supporting a growth-stimulating effect of $\text{KCa3.1}^{\text{high}}$ periodic cells on tumour microtube-connected network neighbours.

Molecular decoding of rhythmic activity

In resected human glioblastoma tissue, tumour cells with detectable KCa3.1 protein expression accounted for 4.8% of all tumour cells in denser network regions but were largely absent in the network-void diffuse invasion zone (Fig. 5a, b and Extended Data Fig. 9a). In single-cell RNA-sequencing data from human tumours, 2.3% of all glioblastoma cells showed detectable KCa3.1 expression (Fig. 5c) and these cells were

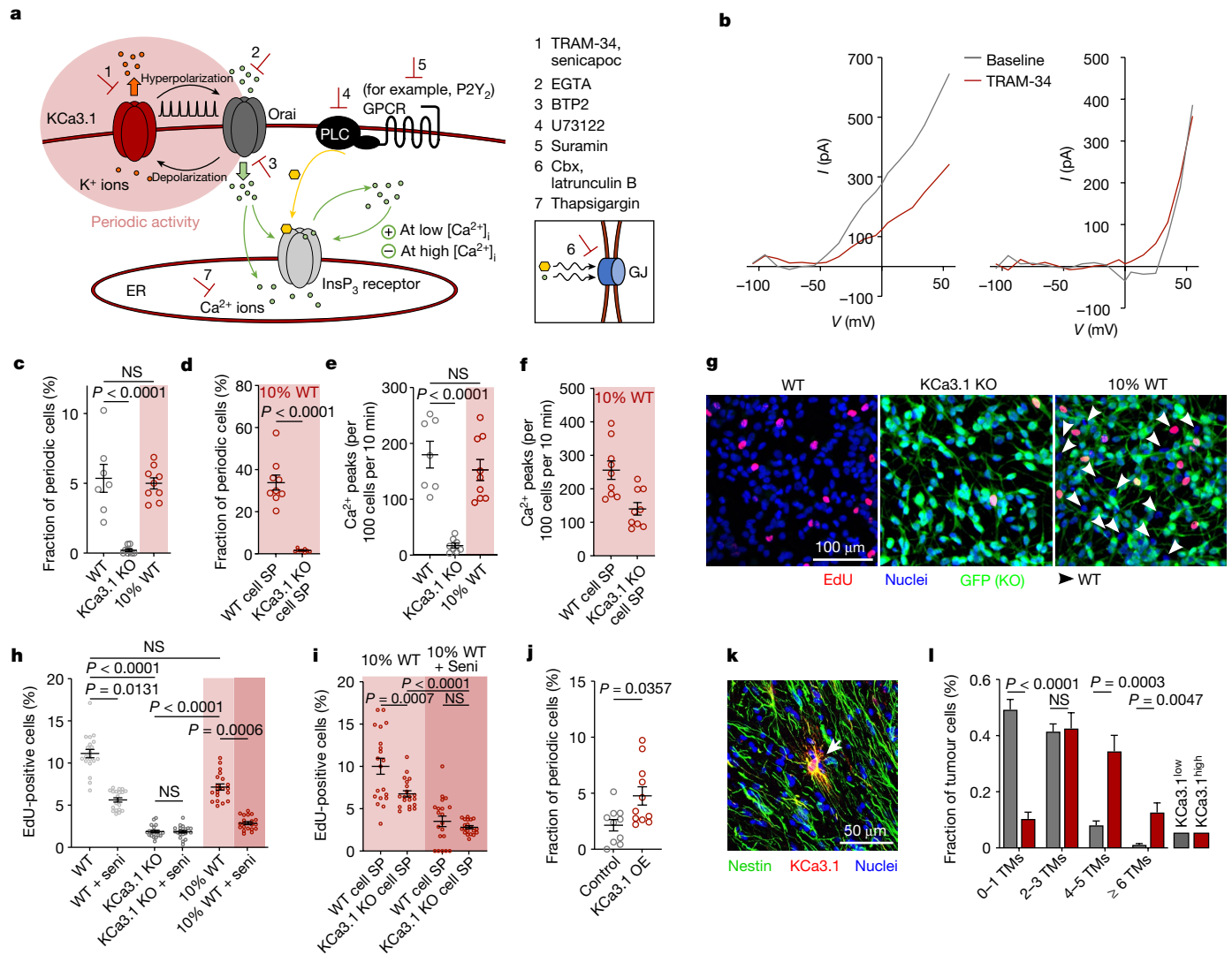


Fig. 4 | KCa3.1 is essential for rhythmic activity. **a**, Schematic summary of main ion fluxes generating or modulating Ca²⁺ oscillations in periodic and other glioblastoma cells, as suggested by the compound screening (see Extended Data Fig. 21–n and the Supplementary Discussion). Inset shows a tumour microtubule. ER, endoplasmic reticulum; GJ, gap junction; GPCR, G-protein-coupled receptor—for example, P2Y₂ purinoreceptor 2; InsP₃, inositol-1,4,5-trisphosphate (yellow hexagons). **b**, Electrophysiological recordings of functional KCa3.1 channels on morphologically particularly network-connected glioblastoma cells. Current (*I*)–voltage (*V*) curves of voltage ramps between –105 mV to 55 mV are shown before (grey trace) and after (red trace) wash-in of 1 μM TRAM-34. TRAM-34-sensitive (left) and TRAM-34-insensitive currents (right) are shown. BG5 line; *n* = 11 cells in total (*n* = 3 sensitive and *n* = 8 insensitive). **c, e**, The fraction of periodic tumour cells among all cells (**c**) and global Ca²⁺ activity in Ca²⁺ recordings of S24 wild-type (WT) cells, S24 KCa3.1-knockout (KO) cells and of a co-culture of 10% S24 wild-type cells with S24 KCa3.1 KO cells (**e**). **d, f**, The fraction of periodic cells among all cells (**d**) and global Ca²⁺ activity of the subpopulation (SP) of S24 wild-type cells and S24 KCa3.1 KO cells in the co-cultures (10% wild type) shown in **c, e**. **c–f**, *n* = 7 recordings (WT), *n* = 8 recordings (KCa3.1 KO) and *n* = 9 recordings (10% WT) in 2

biological independent experiments. One-way ANOVA, Dunnett’s test (**c, e**) and two-sided Mann–Whitney test (**d**). **g, h**, Representative images (**g**) and the fraction of EdU-positive cells in recordings of S24 wild-type cells, S24 KCa3.1 KO cells and a co-culture of 10% S24 wild-type cells with S24 KCa3.1 KO cells after control or 1 μM senicapoc treatment (seni). Arrowheads indicate GFP-negative wild-type cells in co-culture. **i**, The fraction of EdU-positive cells in the subpopulation (SP) of S24 wild-type cells and S24 KCa3.1 KO cells in the respective co-cultures shown in **h** after control or senicapoc treatment. **h, i**, *n* = 20 recordings in 2 biological independent experiments for all groups. Kruskal–Wallis test, Dunn’s test (**h**) and one-way ANOVA, Dunnett’s test (**i**). **j**, The fraction of periodic cells among all active cells in Ca²⁺ recordings of KCa3.1 overexpression (OE) versus control. S24 line in vitro; *n* = 10 recordings (control) and *n* = 11 recordings (KCa3.1 OE) from 2 biologically independent experiments per group. Two-sided Mann–Whitney test. **k, l**, Representative nestin and KCa3.1 immunofluorescence in tumours growing in mice (**k**) and the fraction of tumour cells with the respective number of tumour microtubules (TMs) per tumour cell in KCa3.1^{high} and KCa3.1^{low} cells in vivo (**l**). BG5 line; *n* = 21 regions in 3 mice. Repeated measures one-way ANOVA, Holm–Šidák test. Data are mean ± s.e.m.

enriched in the mesenchymal-like subpopulation (Fig. 5c,d). These numbers match the preclinical frequencies of KCa3.1^{high} cells (Extended Data Fig. 8e) and cells displaying periodic Ca²⁺ activity (Fig. 2b). Consistently, in single-cell RNA-sequencing data of glioblastoma cells xenografted in mice, 1.4% of all cells expressed KCa3.1 above the detection limit and were enriched in the network-connected tumour cell subpopulation (Fig. 5e). Ingenuity pathway analysis (IPA) and gene set

enrichment analysis (GSEA) of KCa3.1^{high} cells and tumours with high expression of KCa3.1 in RNA-expression datasets of human glioblastoma revealed a consistent signature that involved the upregulation of cell-to-cell signalling, outgrowth of protrusions, proliferation, survival and downregulation of cell death (Extended Data Fig. 9b–g).

We next investigated how glioblastoma cells translate the network’s rhythmic Ca²⁺ oscillations into biological information. Multiple key

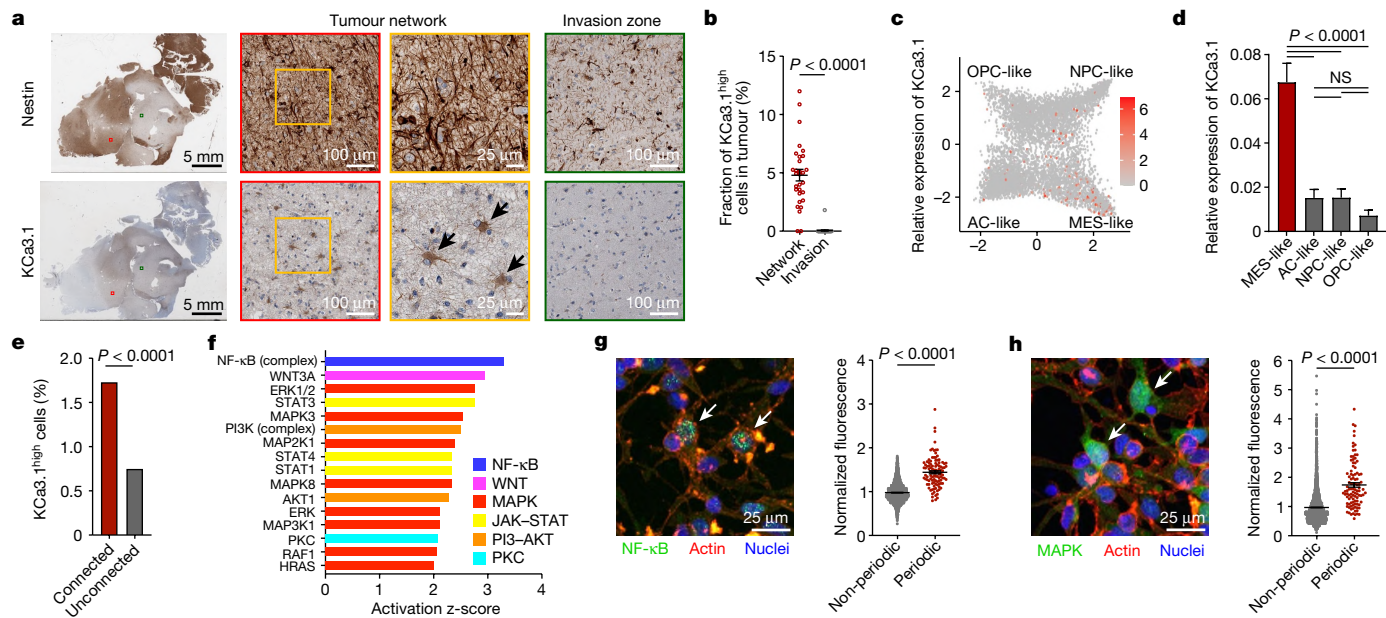


Fig. 5 | KCa3.1 expression in human glioblastomas and molecular decoding of intrinsic rhythmicity. **a**, Immunostaining of Nestin and KCa3.1 in a human glioblastoma sample of a representative tumour network region and invasion zone. Squares indicate the location of the region enlarged immediately to the right. Arrows indicate KCa3.1^{high} cells. $n = 3$ samples from different patients. **b**, The fraction of KCa3.1^{high} tumour cells in the tumour network and the invasion zone of human glioblastoma samples. $n = 30$ regions of interest (ROIs) (tumour network) and $n = 30$ ROIs (invasion zone) in 3 samples from different patients. Two-sided Mann–Whitney test. **c, d**, Two-dimensional representation (c) and KCa3.1 expression values (log transcripts per million (TPM)) (d) of cellular states from 28 patients with glioblastoma³⁸. OPC-like, oligodendrocyte progenitor-like; NPC-like, neural progenitor-like; AC-like, astrocyte-like; MES-like, mesenchymal-like. $n = 1,047$ cells per group. Kruskal–Wallis test,

Dunn’s test. **e**, The fraction of KCa3.1^{high} cells in connected versus unconnected cells from three xenograft single-cell RNA-sequencing datasets (S24, T269 and P3 line); $n = 24,160$ cells (connected) and $n = 11,662$ cells (unconnected). Fisher’s exact test. **f**, Activation z-score of the top activated signalling pathways derived from Ingenuity Pathway Analysis (IPA) using the differential gene expression of KCa3.1^{high} versus KCa3.1^{low} cells in a single-cell RNA-sequencing dataset of 28 glioblastomas³⁸. **g, h**, Representative phospho-NF- κ B (Ser536) (g) and phospho-p44/42 MAPK (Thr202/Tyr204) (h) immunofluorescence and quantification. Arrows indicate cells that displayed periodic Ca²⁺ oscillations in the preceding Ca²⁺ recording. S24 line; $n = 2,348$ cells (non-periodic, NF- κ B), $n = 107$ (periodic, NF- κ B), $n = 2,475$ cells (non-periodic, MAPK) and $n = 101$ (periodic, MAPK) from 2 biologically independent experiments. Two-sided Mann–Whitney test. Data are mean \pm s.e.m.

intracellular signalling pathways have Ca²⁺ frequency decoding properties: they are specifically activated by distinct frequencies over a wide range^{20–22} between 0.5–10⁵ mHz. The frequencies of the intrinsically rhythmic Ca²⁺ activity of glioblastoma cell networks (mean: 12.5–12.7 mHz in vivo and 9.7–11.3 mHz in vitro; Fig. 2c) lie in the same range in which the MAPK and NF- κ B pathways that enhance proliferation and cell survival^{123,24} are maximally activated^{20,25,26}. Indeed, the most upregulated signalling pathways in KCa3.1^{high} cells and tumours with a high expression of KCa3.1 in RNA-expression datasets of human glioblastoma included these two pathways, whereas the CaMKII and calpain pathways that are activated by considerably higher Ca²⁺ spike frequencies^{20,27,28} around 1–50 Hz were not upregulated (Fig. 5f and Extended Data Fig. 9h,i). Furthermore, immunocytochemistry of cells displaying periodic Ca²⁺ activity showed activation of the MAPK and NF- κ B pathways (Fig. 5g,h) but not of the CaMKII and calpain pathways (Extended Data Fig. 9j,k), and inhibiting periodic Ca²⁺ activity with the KCa3.1 blocker senicapoc led to specific downregulation of the MAPK and NF- κ B pathways (Extended Data Fig. 9l–n). Finally, genetic overexpression of KCa3.1 increased (Extended Data Fig. 9o,p) and its knockout reduced (Extended Data Fig. 9q,r) the global activity of MAPK and NF- κ B pathways. Again, we were able to rescue the effect of the knockout by co-culturing KCa3.1-knockout cells with a small fraction of wild-type cells, increasing the activity of the MAPK and NF- κ B pathways in the entire network and in the subpopulation of knockout cells (Extended Data Fig. 9q–s).

KCa3.1 perturbation slows glioma growth

To further validate the biological and potential therapeutic relevance of KCa3.1-related autonomous rhythmic network activity for brain

tumours, we treated tumour-bearing mice with the KCa3.1 inhibitors TRAM-34 and senicapoc, which cross the blood-brain barrier and are well tolerated^{14,15,29,30}. Senicapoc has also been demonstrated to be safe in clinical trials for non-oncological diseases³¹. In accordance with the monolayer and organoid data described above, KCa3.1 inhibition reduced the fraction of periodic cells in experimental gliomas growing in the mouse brain, resulting in strongly reduced global Ca²⁺ activity (Fig. 6a,b and Supplementary Video 5), but did not affect cellular communication per se (Extended Data Fig. 10a). In addition to the known reduction of tumour cell invasion and microglia activation under KCa3.1 inhibition^{15,16,32,33} (Extended Data Fig. 10b–f), TRAM-34 and senicapoc treatments over 14 days also significantly inhibited glioblastoma cell proliferation (Extended Data Fig. 10g–j) and overall tumour growth (Fig. 6c,d and Extended Data Fig. 10k–m). Finally, chronic oral administration of the KCa3.1 inhibitor senicapoc in a moderate, well-tolerated dose attenuated the growth of well-established tumours in mice and extended host survival (Fig. 6e–g). To confirm that selective interference in KCa3.1-dependent periodic activity driven by a small percentage of glioblastoma network cells is responsible for the antitumour effects, we implanted glioblastoma cells with genetic KCa3.1 knockdown to prevent normal autonomous rhythmic Ca²⁺ activity (Extended Data Fig. 6b) into mouse brains. MRI analysis showed a marked reduction of tumour growth in these mice, which resulted in their extended survival (Fig. 6h–j).

To further support the relevance of these findings for human disease, we analysed survival in relation to KCa3.1 expression. KCa3.1 expression was significantly higher in glioblastoma than in prognostically more favourable glioma types (Extended Data Fig. 10n). Analysis of a cohort of patients with glioblastoma from The Cancer Genome Atlas

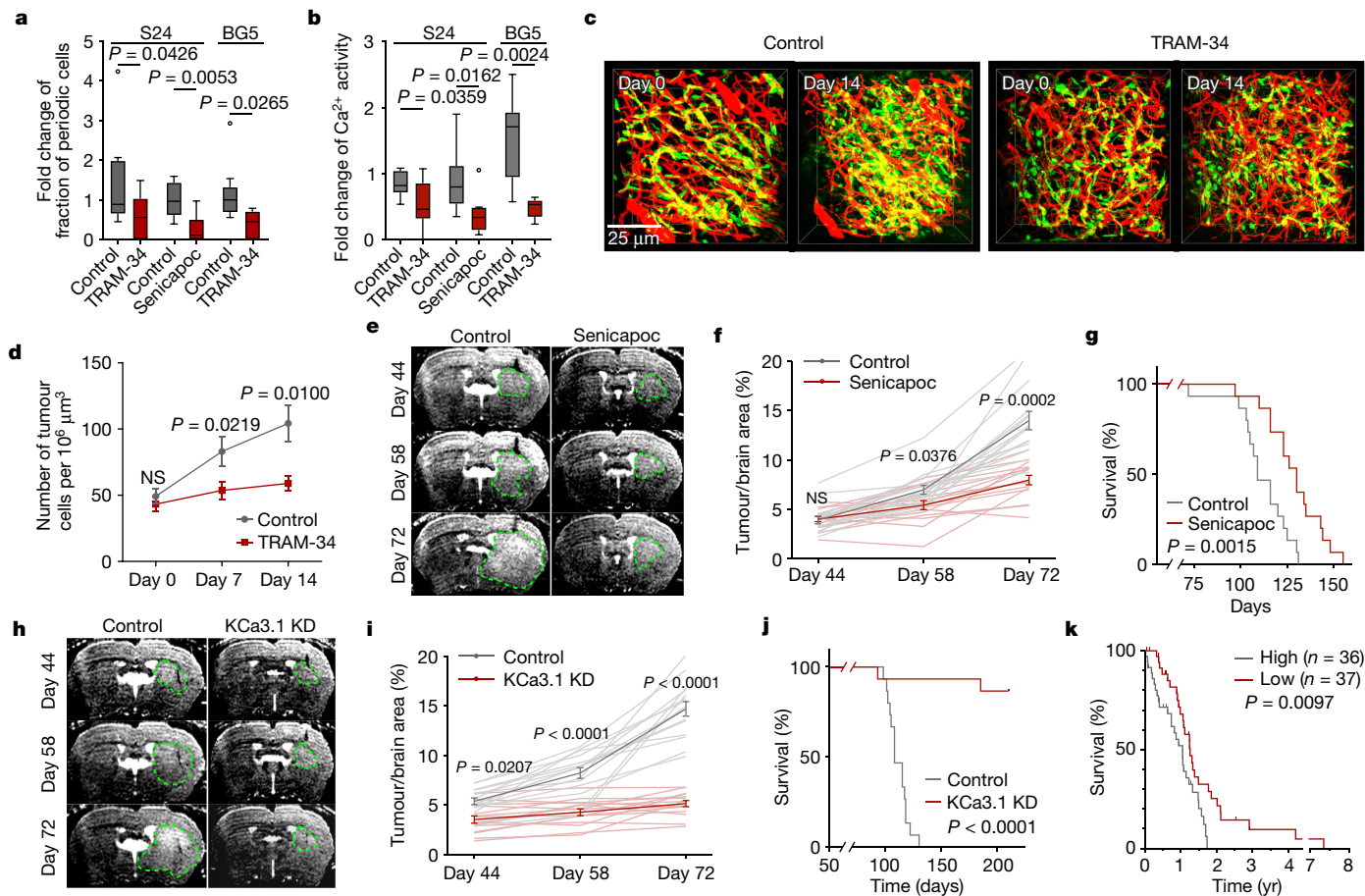


Fig. 6 | Targeting KCa3.1 reduces brain tumour growth. **a, b**, Fold change in the fraction of periodic cells among all active cells (**a**) and fold change of global Ca^{2+} activity in Ca^{2+} recordings (**b**) from control, TRAM-34 (intraperitoneal injection, 120 mg per kg body weight) or senicapoc (intraperitoneal injection, 50 mg per kg body weight) treated mice. $n = 9$ (control) and $n = 12$ (TRAM-34) recordings in 4 mice in S24 cell line; $n = 8$ recordings in 4 mice (control and senicapoc) in S24 cell line; $n = 9$ recordings in 4 mice (control) and $n = 5$ recordings in 3 mice (TRAM-34) in BG5 cells. Kruskal–Wallis test, Dunn’s test. **c, d**, Representative regions (**c**) and change in cell density (**d**) on day 14 versus day 0 under control conditions versus TRAM-34 treatment (2×120 mg per kg body weight per day). $n = 14$ regions in 4 mice (control) and $n = 21$ regions in

4 mice (TRAM-34). **e–g**, Representative MRI images (**e**), tumour sizes (**f**) and Kaplan–Meier survival plots (**g**) for mice with implanted tumours (S24 line) after senicapoc treatment versus control. Treatment started on day 47 after tumour implantation. $n = 15$ mice per group. One-way ANOVA, Šidák’s test (**f**) and log-rank test (**g**). **h–j**, Representative MRI images (**h**), tumour sizes (**i**) and Kaplan–Meier survival plots (**j**) for mice after implantation of S24 control versus S24 KCa3.1 knockdown (KD) cells. $n = 15$ mice per group. One-way ANOVA, Šidák’s test (**i**) and log-rank test (**j**). **k**, Kaplan–Meier survival plot for patients with glioblastoma in the highest quartile for KCa3.1 expression and those in the lowest quartile for KCa3.1 expression. $n = 36$ patients (high) and $n = 37$ patients (low). log-rank test. Data are mean \pm s.e.m.

(TCGA) revealed increased survival of patients with low KCa3.1 expression, both among the entire patient population (Fig. 6k) and within the prognostically unfavourable mesenchymal disease subgroup in which KCa3.1 was most highly expressed (Extended Data Fig. 10o,p).

Conclusions

Our data suggest that glioblastoma cells organize in resilient networks with scale-free and small-world properties, whose functionality is dependent on a plastic population of cells that display periodic Ca^{2+} activity, often act as functional network hubs and constitute 1–5% of all cells in human samples and mouse models of glioblastoma (Extended Data Fig. 10q). Their distinct autonomous activity generates network-wide rhythmic intercellular Ca^{2+} waves that specifically activate the MAPK and NF- κ B pathways and ultimately drive brain tumour growth. The network’s fundamental dependence on intrinsically rhythmic cells creates a previously unknown vulnerability⁷. We show here that this crucial cellular state in glioblastoma can be effectively targeted by brain-penetrant KCa3.1 inhibitors, revealing a new class of drugs against incurable brain tumours.

Although our experiments have not demonstrated that tumour cells displaying this distinct activity are a stable cell population of classic pacemakers (such as in the sinoatrial node of the heart where KCa3.1 is involved in pacemaking, but with limited functional importance³⁴), they nevertheless show many similarities to the function, plasticity and biological role of pacemaker-like cells during neurodevelopment³⁵. Our findings enable a more comprehensive understanding of the brain tumour ‘organism’: whereas its invasive front that colonizes new brain regions is driven by a subpopulation of isolated glioblastoma cells with distinct neuronal features³⁶, the more established population is governed by a very small subpopulation of mesenchymal-like glioblastoma cells that nonetheless recapitulates other neurodevelopmental features, and that is of crucial importance for the functionality and resilience of the tumour cell network that resists established antitumour therapies^{2,8}.

It will be valuable to determine whether intrinsically rhythmic glioblastoma cells also exhibit the increased tumorigenicity and plasticity that have been associated with cancer stem-like cells. Whatever the results are, the presence of periodically active network hubs extends our understanding of how a small subpopulation of cancer cells can dictate the functionality of the entire tumour.

1. Weller, M. et al. Glioma. *Nat. Rev. Dis. Primers* **1**, 15017 (2015).
2. Osswald, M. et al. Brain tumour cells interconnect to a functional and resistant network. *Nature* **528**, 93–98 (2015).
3. Venkataramani, V. et al. Glutamatergic synaptic input to glioma cells drives brain tumour progression. *Nature* **573**, 532–538 (2019).
4. Venkatesh, H. S. et al. Electrical and synaptic integration of glioma into neural circuits. *Nature* **573**, 539–545 (2019).
5. Gritsenko, P. G. et al. p120-catenin-dependent collective brain infiltration by glioma cell networks. *Nat. Cell Biol.* **22**, 97–107 (2020).
6. Winkler, F. & Wick, W. Harmful networks in the brain and beyond. *Science* **359**, 1100–1101 (2018).
7. Albert, R., Jeong, H. & Barabasi, A. L. Error and attack tolerance of complex networks. *Nature* **406**, 378–382 (2000).
8. Weil, S. et al. Tumor microtubules convey resistance to surgical lesions and chemotherapy in gliomas. *Neuro Oncol.* **19**, 1316–1326 (2017).
9. Lee, J. et al. Tumor stem cells derived from glioblastomas cultured in bFGF and EGF more closely mirror the phenotype and genotype of primary tumors than do serum-cultured cell lines. *Cancer Cell* **9**, 391–403 (2006).
10. Watts, D. J. & Strogatz, S. H. Collective dynamics of ‘small-world’ networks. *Nature* **393**, 440–442 (1998).
11. Barabasi, A. L. & Albert, R. Emergence of scaling in random networks. *Science* **286**, 509–512 (1999).
12. Milo, R. et al. Network motifs: simple building blocks of complex networks. *Science* **298**, 824–827 (2002).
13. Dupont, G., Combettes, L., Bird, G. S. & Putney, J. W. Calcium oscillations. *Cold Spring Harb. Perspect. Biol.* **3**, a004226 (2011).
14. Chen, Y. J. et al. The potassium channel KCa3.1 constitutes a pharmacological target for neuroinflammation associated with ischemia/reperfusion stroke. *J. Cereb. Blood Flow Metab.* **36**, 2146–2161 (2016).
15. D’Alessandro, G. et al. KCa3.1 channels are involved in the infiltrative behavior of glioblastoma in vivo. *Cell Death Dis.* **4**, e773 (2013).
16. Turner, K. L., Honasoge, A., Robert, S. M., McFerrin, M. M. & Sontheimer, H. A proinvasive role for the Ca²⁺-activated K⁺ channel KCa3.1 in malignant glioma. *Glia* **62**, 971–981 (2014).
17. Ruggieri, P. et al. The inhibition of KCa3.1 channels activity reduces cell motility in glioblastoma derived cancer stem cells. *PLoS ONE* **7**, e47825 (2012).
18. D’Alessandro, G. et al. KCa3.1 channel inhibition sensitizes malignant gliomas to temozolomide treatment. *Oncotarget* **7**, 30781–30796 (2016).
19. Wang, H. Y. et al. A three ion channel genes-based signature predicts prognosis of primary glioblastoma patients and reveals a chemotherapy sensitive subtype. *Oncotarget* **7**, 74895–74903 (2016).
20. Smedler, E. & Uhlen, P. Frequency decoding of calcium oscillations. *Biochim. Biophys. Acta* **1840**, 964–969 (2014).
21. Parekh, A. B. Decoding cytosolic Ca²⁺ oscillations. *Trends Biochem. Sci.* **36**, 78–87 (2011).
22. Wacquier, B., Voorluis, V., Combettes, L. & Dupont, G. Coding and decoding of oscillatory Ca²⁺ signals. *Semin. Cell Dev. Biol.* **94**, 11–19 (2019).
23. Taniguchi, K. & Karin, M. NF- κ B, inflammation, immunity and cancer: coming of age. *Nat. Rev. Immunol.* **18**, 309–324 (2018).
24. Vogelstein, B. et al. Cancer genome landscapes. *Science* **339**, 1546–1558 (2013).
25. Dolmetsch, R. E., Xu, K. & Lewis, R. S. Calcium oscillations increase the efficiency and specificity of gene expression. *Nature* **392**, 933–936 (1998).
26. Kupzig, S., Walker, S. A. & Cullen, P. J. The frequencies of calcium oscillations are optimized for efficient calcium-mediated activation of Ras and the ERK/MAPK cascade. *Proc. Natl Acad. Sci. USA* **102**, 7577–7582 (2005).
27. Eshete, F. & Fields, R. D. Spike frequency decoding and autonomous activation of Ca²⁺-calmodulin-dependent protein kinase II in dorsal root ganglion neurons. *J. Neurosci.* **21**, 6694–6705 (2001).
28. Tompa, P., Tóth-Boconádi, R. & Friedrich, P. Frequency decoding of fast calcium oscillations by calpain. *Cell Calcium* **29**, 161–170 (2001).
29. Jin, L. W. et al. Repurposing the KCa3.1 inhibitor senicapoc for Alzheimer’s disease. *Ann. Clin. Transl. Neurol.* **6**, 723–738 (2019).
30. Staal, R. G. W. et al. Inhibition of the potassium channel K_{Ca}3.1 by senicapoc reverses tactile allodynia in rats with peripheral nerve injury. *Eur. J. Pharmacol.* **795**, 1–7 (2017).
31. Ataga, K. I. et al. Improvements in haemolysis and indicators of erythrocyte survival do not correlate with acute vaso-occlusive crises in patients with sickle cell disease: a phase III randomized, placebo-controlled, double-blind study of the Gardos channel blocker senicapoc (ICA-17043). *Br. J. Haematol.* **153**, 92–104 (2011).
32. Maezawa, I., Jenkins, D. P., Jin, B. E. & Wulff, H. Microglial KCa3.1 channels as a potential therapeutic target for Alzheimer’s disease. *Int. J. Alzheimers Dis.* **2012**, 868972 (2012).
33. Kaushal, V., Koeberle, P. D., Wang, Y. & Schlichter, L. C. The Ca²⁺-activated K⁺ channel KCNN4/KCa3.1 contributes to microglia activation and nitric oxide-dependent neurodegeneration. *J. Neurosci.* **27**, 234–244 (2007).
34. Weisbrod, D. et al. SK4 Ca²⁺ activated K⁺ channel is a critical player in cardiac pacemaker derived from human embryonic stem cells. *Proc. Natl Acad. Sci. USA* **110**, E1685–E1694 (2013).
35. Blankenship, A. G. & Feller, M. B. Mechanisms underlying spontaneous patterned activity in developing neural circuits. *Nat. Rev. Neurosci.* **11**, 18–29 (2010).
36. Venkataramani, V. et al. Glioblastoma hijacks neuronal mechanisms for brain invasion. *Cell* **185**, 2899–2917.e2831 (2022).
37. Gerdes, J. et al. Cell cycle analysis of a cell proliferation-associated human nuclear antigen defined by the monoclonal antibody Ki-67. *J. Immunol.* **133**, 1710–1715 (1984).
38. Neftel, C. et al. An integrative model of cellular states, plasticity, and genetics for glioblastoma. *Cell* **178**, 835–849.e821 (2019).

Reporting summary

Further information on research design is available in the Nature Portfolio Reporting Summary linked to this article.

Data availability

Bulk RNA-seq data of connected and unconnected glioma cells have been deposited in the Sequence Read Archive (SRA) database under accession number PRJNA554870. Bulk RNA-seq data of cells treated with senicapoc and control have been deposited in the Gene Expression Omnibus under accession number GSE215365. Source data are provided with this paper.

Code availability

The code supporting the current study has been deposited in Zenodo at <https://doi.org/10.5281/zenodo.7242228>.

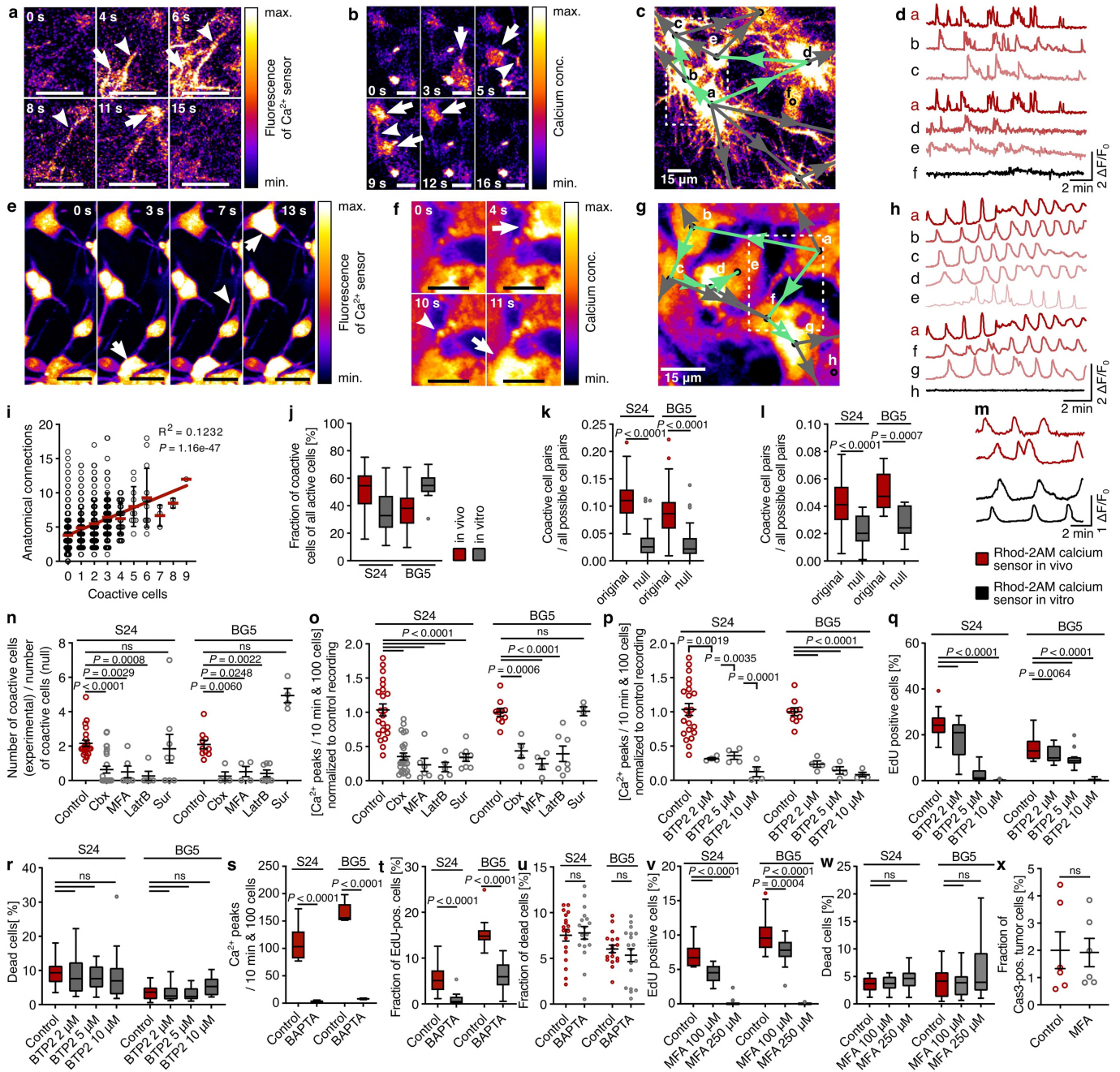
Acknowledgements We thank K. Frey for technical assistance and M. Fischer for acquiring the MRI images; O. Bracko for the training in cranial window preparation and in vivo multi-photon imaging; A. Schulz and M. Vogel for RNA-sequencing services; and M. Brom and D. Kronic for their help with confocal microscopy. This work was supported by the Deutsche Forschungsgemeinschaft (SFB 1389, UNITE Glioblastoma, project ID 404521405, to W.W., F.W., E.J., T. Kessler, M.O.B., M.R., F.S., and M.S., and Emmy Noether programme DFG to M.O.B., BR 6153/1-1), the Heinrich F. C. Behr Foundation to D.H. and the German Research Foundation (VE1373/2-1), Else Kröner-Fresenius-Stiftung (2020-EKEA.135), the Stiftung SET to F.W. P.K. and the University of Heidelberg (Physician Scientist-Programm and Krebs- und Scharlachstiftung) to V.V., and the Bundesministerium für Bildung und Forschung within the framework of the e.Med research and funding concept to M.A.K. (01ZX1913D).

Author contributions D.H. designed, conducted and analysed experiments and contributed to all aspects of the study, in particular confocal and in vivo multi-photon imaging of glioma network activity, proliferation, and invasion, immunofluorescence, immunochemistry,

cranial window implantation, tumour implantation, quantification and analysis of the data, data interpretation, writing the code, TCGA data and RNA-expression data analysis. D.H. initially discovered the intrinsically rhythmic cells. D.H. and F.W. wrote the manuscript with the input of all co-authors. D.C.H. performed sample preparation and transcriptional analyses. D.C.H., V.V. and E.J. provided conceptual and methodological input and data interpretation. V.V. and S.K.T. performed electrophysiological recordings under the supervision of T. Kuner. S.H. and A.J. conducted brain organoid experiments under the supervision of P.K. D.D.A. and S. Weil performed cranial window implantation and tumour injections and provided conceptual input. L.H. and T. Kessler performed bioinformatic analysis of RNA-expression data. T. Kessler provided conceptual input. A.K. provided the KCa3.1-knockout constructs. P.S. and A.H. provided staining of human paraffin sections under the supervision of F.S. M.O.B. provided MRI and subsequent analysis. M.A.K. and M.R. provided conceptual input. J.M.M., Y.Y. and E.R. performed tumour injections. S. Wendler and C.L. performed cell culture work, C.L. and C.M. performed immunostaining. K.F. and O.G. provided the Twitch-3A vector. M.O. provided in vivo Ca²⁺ imaging data and conceptual input. G.S. performed in vivo Ca²⁺ imaging. M.S. provided conceptual input for network analyses. W.W. provided conceptual input, performed data interpretation and supervised RNA-expression data analysis. F.W. conceptualized and supervised all aspects of the study and performed data interpretation.

Competing interests E.J., M.O., W.W. and F.W. are inventors on patent no. WO2017020982A1 titled 'Agents for Use in the Treatment of Glioma'. F.W. reports a research collaboration with DC Europa Limited, GlaxoSmithKline, Genentech and Boehringer. F.W. is co-founder of DC Europa Limited. M.R. reports a research grant from Novocure and honoraria, consulting fees and lecture fees from Novocure and Alexxion (now AstraZeneca). G.S. is an employee of Carl Zeiss Microscopy GmbH. F.S. received honoraria from Bayer and Illumina. W.W. is an inventor and patent holder on 'Peptides for use in Treating or Diagnosing IDH1R132H Positive Cancers' (patent no. EP2800580B1) and 'Cancer Therapy with an Oncolytic Virus Combined with a Checkpoint Inhibitor' (US11027013B2). He has consulted for Apogenix, AstraZeneca, Bayer, Enterome, Medac, MSD and Roche/Genentech, with honoraria paid to the Medical Faculty at the University of Heidelberg.

Correspondence and requests for materials should be addressed to Frank Winkler.

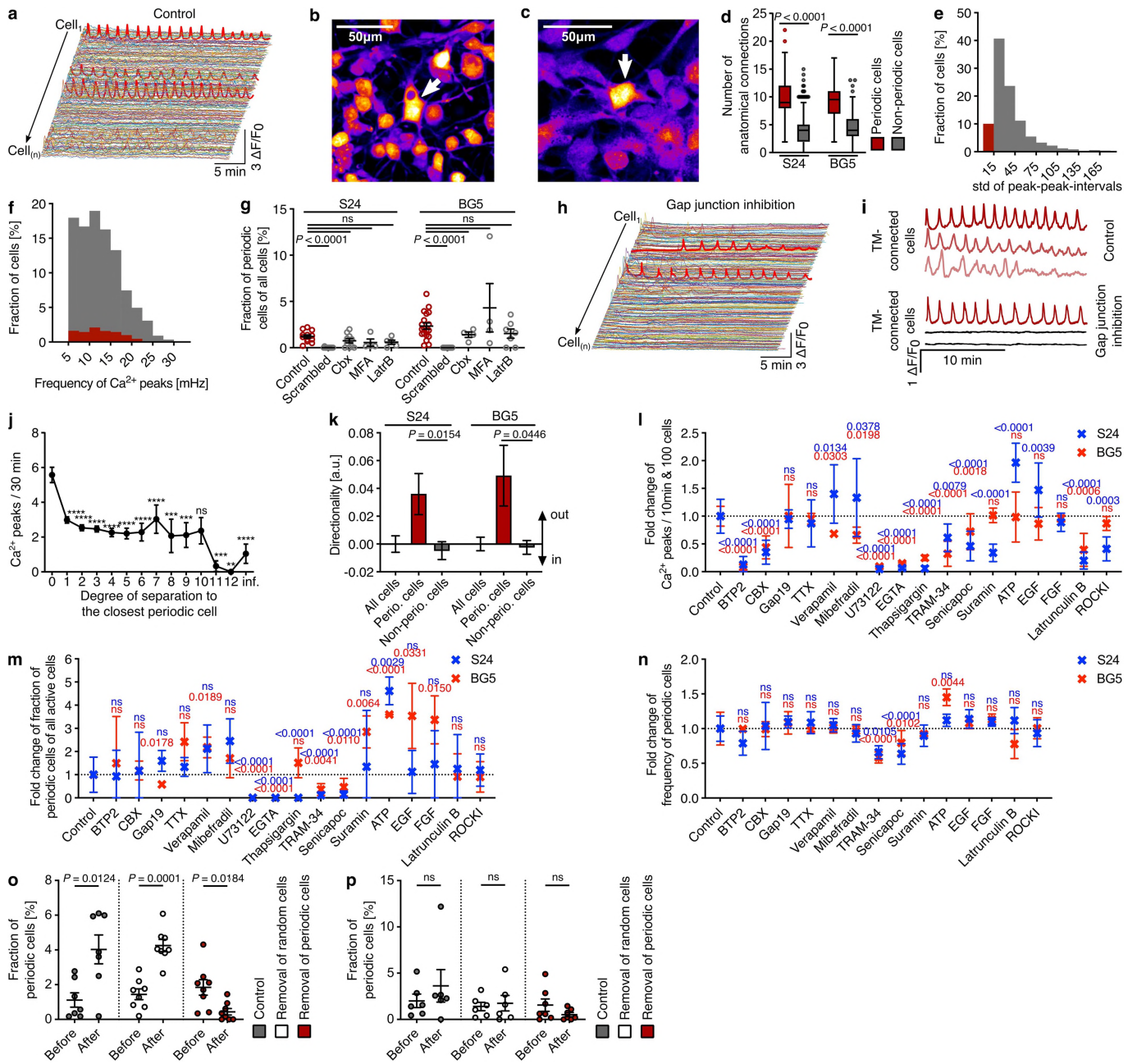


Extended Data Fig. 1 | See next page for caption.

Extended Data Fig. 1 | Glioblastoma network communication depends on

TMs and gap junctions and drives tumor cell proliferation. a, b, Time-lapse images of Ca^{2+} transients travelling between two glioblastoma cells along a TM in the mouse brain *in vivo*; S24 line (a) and BG5 line (b); scale bars are 25 μm (a) and 15 μm (b); region of a is indicated in Fig. 1a, region of b is indicated in c by dotted box; arrows denote Ca^{2+} peaks in cell somata; arrowheads denote intercellular Ca^{2+} transient traveling through TMs. **c,** Network plot of coactive cell pairs derived from Ca^{2+} recordings of BG5 tumor cells; arrowheads indicate the direction of the transients. **d,** Synchronized Ca^{2+} transients of TM-connected tumor cells. Red: Ca^{2+} transients detectable; black: no Ca^{2+} peaks detectable. **e,** same as (a), but with a novel *in vitro* tumor cell network growth assay; S24 line; scale bar is 25 μm ; region is indicated in Fig. 1c. **f–h,** same as b–d, but with a novel *in vitro* tumor cell network growth assay; scale bar in d is 15 μm . **i,** Number of coactive cells versus number of anatomical connections per cell; S24 line *in vitro*, $n = 1602$ cells from 4 recordings and 2 biologically independent experiments; linear regression. **j,** Fraction of cells with at least one coactive cell out of all active cells (here and below cells with ≥ 4 Ca^{2+} peaks). **k, l,** Normalized fraction of coactive cell pairs in *in vivo* (k) and *in vitro* (l) data and its corresponding null control; Kruskal-Wallis test, Dunn's test for *in vivo* data and one-way ANOVA, Dunnett's test for *in vitro* data; **j–l,** $n = 23$ recordings from 3 mice (S24 *in vivo*), $n = 22$ recordings from 9 biologically independent experiments (S24 *in vitro*), $n = 40$ recordings from 4 mice (BG5 *in vivo*), and $n = 10$ recordings from 5 biologically independent experiments (BG5 *in vitro*). **m,** Representative traces of Ca^{2+} transients of cells stained with Rhod-2AM and imaged with multiphoton microscopy *in vivo* and confocal microscopy *in vitro* (see Methods for more information); note that Ca^{2+} peak morphology is very similar *in vivo* and *in vitro* when the same Ca^{2+} sensor and similar recording technologies are used. **n,** Intercellular coactivity in Ca^{2+} recordings of control versus 100 μM Carbenoxolone (Cbx, gap junction inhibition), 100 μM MFA (gap junction inhibition), 1 μM Latrunculin B (LatrB, reduction of TM growth), and 100 μM Suramin (purinergic receptor inhibition) treatment *in vitro*; intercellular coactivity was calculated by dividing the number of coactive cells of a recording by the number of coactive cells of its corresponding null control data; note that the inhibition of extracellular transfer of ATP by Suramin increased the intercellular coactivity, possibly by reducing extracellular noise, and thereby revealing the pure, TM-mediated and highly synchronized Ca^{2+} -mediated communication of the tumor cells; Kruskal-Wallis test, uncorrected Dunn's test. **o,** Normalized global Ca^{2+} activity in control versus 100 μM Carbenoxolone (Cbx), 100 μM MFA, 1 μM Latrunculin B (LatrB), and 100 μM Suramin treatment *in vitro*; global calcium activity (number of Ca^{2+} peaks per time and cell) was normalized by dividing the number of peaks per cell and time by the mean of the corresponding control recording; one-way ANOVA,

Dunnett's test. **n, o,** $n = 22$ recordings (S24; control), $n = 25$ recordings (S24; Cbx), $n = 6$ recordings (S24; MFA), $n = 5$ recordings (S24; LatrB), $n = 8$ recordings (S24; Sur), $n = 10$ recordings (BG5; control), $n = 4$ recordings (BG5; Cbx, MFA, and Sur), $n = 7$ recordings (BG5; LatrB) from ≥ 2 biologically independent experiments, respectively. **p,** Normalized global Ca^{2+} activity in control versus SOCE inhibitor BTP2 treatment *in vitro*; $n = 22$ recordings from 9 biologically independent experiments (S24, control), $n = 4$ recordings from 2 biologically independent experiments (S24, 2 μM , 5 μM , and 10 μM ; BG5, 2 μM , 5 μM , and 10 μM); one-way ANOVA, Dunnett's test. **q,** Fraction of EdU-positive cells, measured as number of EdU-positive cells divided by DAPI-positive cells in control versus BTP2 treatment *in vitro*; $n = 26$ recordings (S24; Control and BTP2 2 μM), $n = 23$ recordings (S24; BTP2 5 μM), $n = 29$ recordings (S24; BTP2 10 μM), $n = 27$ recordings (BG5; Control and BTP2 2 μM), and $n = 25$ recordings (BG5; BTP2 5 μM and 10 μM) from 2 biologically independent experiments; one-way ANOVA, Dunnett's test. **r,** Fraction of dead cells, measured as number of PI-positive cells divided by DAPI-positive cells in control versus BTP2 treatment *in vitro*; $n = 18$ recordings (S24; all groups), $n = 24$ recordings (BG5; Control and BTP2 2 μM), $n = 17$ recordings (S24; BTP2 5 μM), $n = 22$ recordings (S24; BTP2 10 μM) from 2 biologically independent experiments; Kruskal-Wallis test, Dunn's test. **s,** Global Ca^{2+} activity in control versus 10 μM BAPTA-AM treatment *in vitro*; $n = 11$ recordings (S24, control), $n = 4$ recordings (S24, BAPTA-AM), $n = 5$ recordings (BG5, control), and $n = 4$ recordings (BG5, BAPTA-AM) from 2 biologically independent experiments; Brown-Forsythe and Welch ANOVA test, Dunnett's test. **t,** Fraction of EdU-positive cells measured as the number of EdU-positive cells divided by DAPI-positive cells in control versus BAPTA-AM treatment *in vitro*; $n = 30$ recordings (S24, control and BAPTA-AM; BG5, control) and $n = 29$ recordings (BG5, BAPTA-AM) from 3 biologically independent experiments; Kruskal-Wallis test, Dunn's test. **u,** Fraction of dead cells, measured as number of PI-positive cells divided by DAPI-positive cells in control versus BAPTA-AM treatment *in vitro*; $n = 18$ recordings (S24, control), $n = 18$ recordings (S24, BAPTA-AM) from 2 biologically independent experiments, $n = 18$ recordings (BG5, control), and $n = 18$ recordings (BG5, BAPTA-AM) from 2 biologically independent experiments; one-way ANOVA, Dunnett's test. **v,** Fraction of EdU-positive cells and **w,** fraction after of dead cells, measured as number of PI-positive cells divided by DAPI-positive cells after control versus MFA treatment (gap junction inhibition) *in vitro*; $n = 18$ recordings per group from 2 biologically independent experiments, respectively; one-way ANOVA, Dunnett's test. **x,** Fraction of activated caspase-3-positive tumor cells in tumor-bearing human cerebral organoids after 14 days of control versus 100 μM MFA treatment; $n = 6$ regions in 3 cerebral organoids per group; S24 line; two-sided Mann-Whitney test. Error bars show s.e.m. ns, not significant ($P \geq 0.05$).

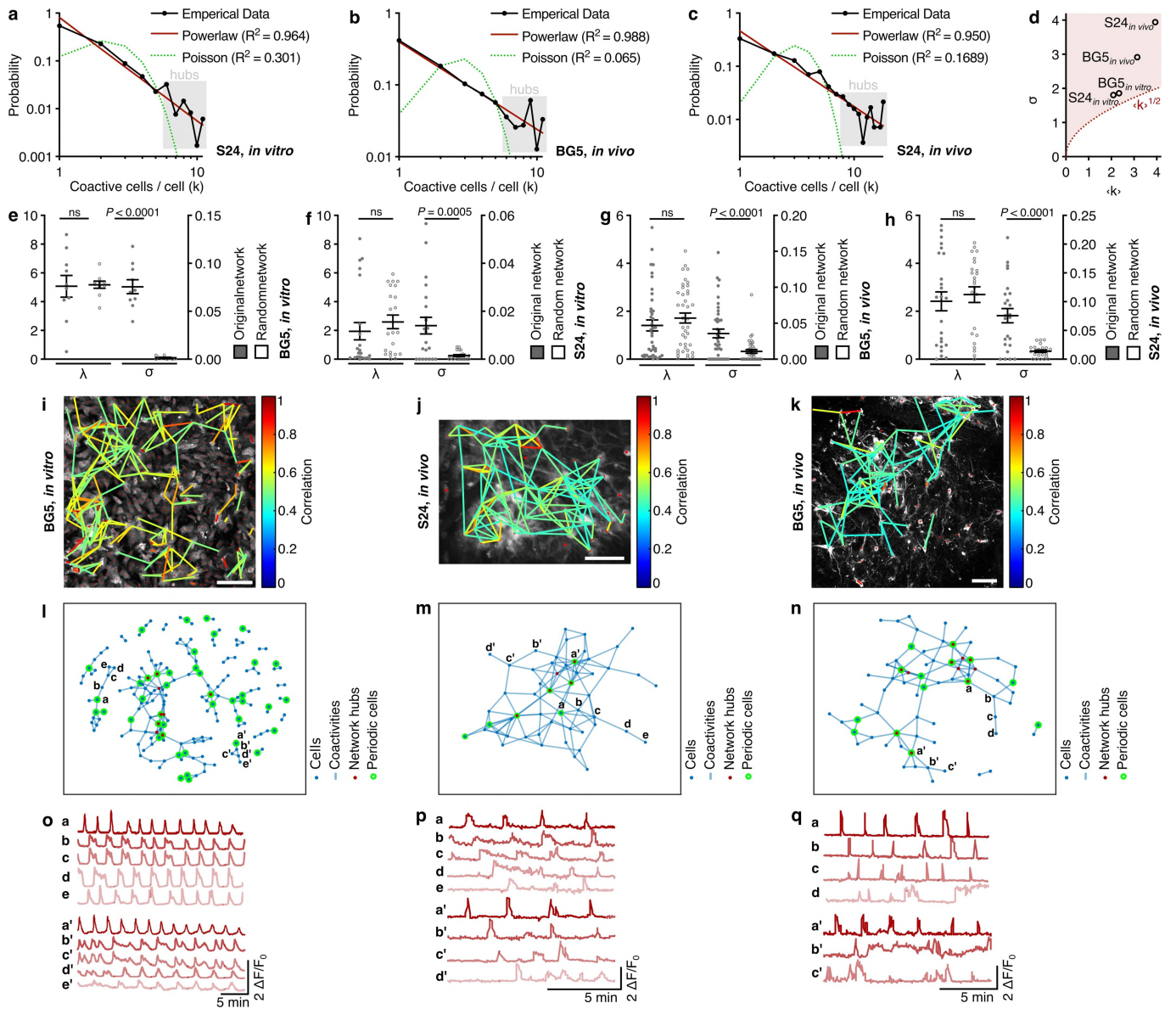


Extended Data Fig. 2 | See next page for caption.

Extended Data Fig. 2 | Characteristics and targeting of periodically active cells.

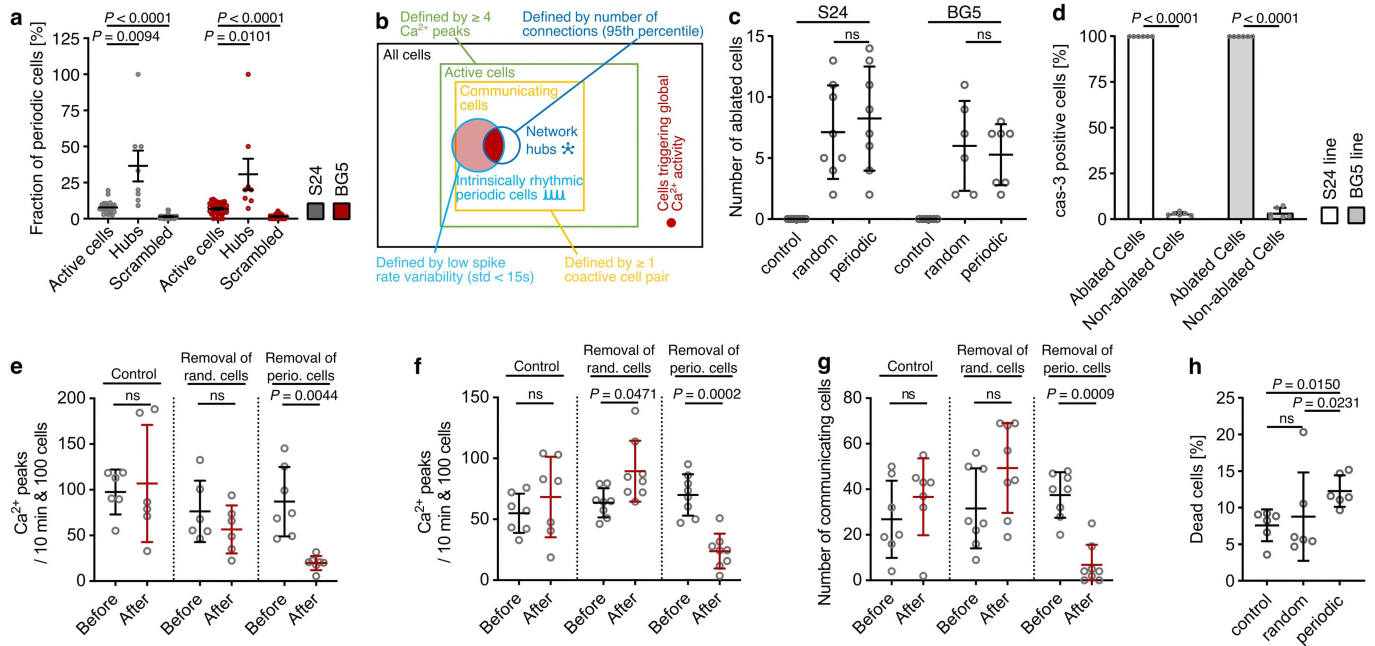
a, Ca^{2+} traces from a representative recording *in vitro*; traces of periodic cells are indicated by thick red lines; BG5 line. **b, c**, Representative recording of S24 (**b**) and BG5 (**c**) tumor cells *in vitro*; arrow indicates typical periodic cell with a high number of anatomical (TM-mediated) cell-cell connections. **d**, Number of TM-mediated cell-cell connections of periodic cells and non-periodic cells *in vitro*. **b–d**, $n = 120$ periodic cells and $n = 1482$ non-periodic cells from 4 recordings from 3 biologically independent experiments (S24); $n = 40$ periodic cells and $n = 1364$ non-periodic cells from 3 recordings from 2 biologically independent experiments (BG5); Kruskal-Wallis test, Dunn's test. **e**, Histogram of the standard deviation (std) of the peak-peak-intervals of all active cells; red bars indicate cells with periodic Ca^{2+} activity; S24 line *in vivo*; $n = 2198$ cells from 24 recordings in 3 mice. **f**, Histograms of the frequency of Ca^{2+} peaks of all active cells; red bars indicate cells with periodic Ca^{2+} activity; $n = 2198$ cells (S24 *in vivo*) from 24 recordings in 3 mice. **g**, Fraction of periodic cells of all cells in empirical (control) and scrambled data versus 100 μM Carbenoxolone (Cbx; gap junction inhibition), 100 μM MFA (gap junction inhibition), and 1 μM Latrunculin B (LatrB; reduction of TM growth) treatment *in vitro*; $n = 12$ recordings (S24; control), $n = 10$ recordings (S24; Cbx), $n = 4$ recordings (S24; MFA), $n = 5$ recordings (S24; LatrB), $n = 19$ recordings (BG5; control), $n = 4$ recordings (BG5; Cbx, MFA), $n = 7$ recordings (BG5; LatrB) from $n \geq 2$ independent experiments, respectively; Kruskal-Wallis test, Dunn's test. **h**, Ca^{2+} traces from a representative recording after gap junction inhibition with 100 μM MFA *in vitro*; traces of periodic cells are indicated by thick red lines; BG5 line. **i**, Representative Ca^{2+} transients of periodic cells (dark red, upper lines) and anatomically connected non-periodic cells (lighter red and black) *in vitro*; S24 line. **j**, Number of Ca^{2+} peaks of all cells as a function of the degree of separation to the closest periodic cell, which corresponds to the number of cell-cell connections between the cell and the closest periodic cell *in vitro*; BG5 line; $n = 40$ cells (0), $n = 297$ cells (1), $n = 320$ cells (2), $n = 304$ cells (3), $n = 196$ cells (4), $n = 98$ cells (5), $n = 48$ cells (6), $n = 31$ cells (7), $n = 14$ cells (8), $n = 17$ cells (9), $n = 11$ cells (10), $n = 6$ cells (11), $n = 3$ cells (12), $n = 20$ cells (inf.) from 3 recordings from 3 independent

experiments; Kruskal-Wallis test, Dunn's test; $***P < 0.01$; $****P < 0.001$; $****P < 0.0001$. **k**, Directionality of the Ca^{2+} signals between communicating cells for periodic cells and non-periodic cells *in vitro*; $n = 555$ periodic cells and $n = 2719$ non-periodic cells from 22 recordings from 9 biologically independent experiments (S24) and $n = 189$ periodic cells and $n = 3291$ non-periodic cells from 10 recordings from 5 biologically independent experiments (BG5); Kruskal-Wallis test, Dunn's test. **l**, Fold change of global Ca^{2+} activity, **m**, fold change of fraction of periodic cells of all active cells, and **n**, fold change of frequency of Ca^{2+} oscillations of periodic cells after control ($n = 49$ and $n = 22$) versus BTP2 ($n = 4$ and $n = 4$), Cbx ($n = 9$ and $n = 4$), Gap19 ($n = 4$ and $n = 3$), TTX ($n = 4$ and $n = 3$), Verapamil ($n = 4$ and $n = 3$), Mibefradil ($n = 4$ and $n = 3$), U73122 ($n = 2$ and $n = 3$), EGTA ($n = 2$ and $n = 3$), Thapsigargin ($n = 2$ and $n = 3$), TRAM-34 ($n = 5$ and $n = 5$), Senicapoc ($n = 12$ and $n = 11$), Suramin ($n = 8$ and $n = 4$), ATP ($n = 4$ and $n = 3$), EGF ($n = 4$ and $n = 4$), FGF ($n = 3$ and $n = 4$), Latrunculin B ($n = 5$ and $n = 7$), and Y-27632 (ROCK1) ($n = 4$ and $n = 4$) treatment *in vitro*; see the Supplementary Discussion for mechanistic insights and Methods for respective concentrations; U73122, EGTA, Thapsigargin were not included in (**n**), as there was no Ca^{2+} activity in the presence of these drugs and therefore no periodic cells were detected; error bars show s.d.; 'n' is provided for S24 and BG5, respectively from $n \geq 2$ independent experiments per group; one-way ANOVA, Uncorrected Fisher's LSD (**l**) and Brown-Forsythe and Welch ANOVA, Dunnett's test (**m, n**). **o, p**, Fraction of periodic cells of all cells before and after laser ablation; after laser ablation of random cells the number of periodic cells increased (only significant in **o**) and after laser ablation of all periodic cells, the number of periodic cells was not zero as expected, because new periodic cells appeared in the recordings, that were, however, not able to compensate the loss of the previous periodic cells (Fig. 3h, i, Extended Data Fig. 4f–h); S24 line (**o**) and BG5 line (**p**); $n = 6$ recordings (BG5 control and random), $n = 7$ (S24 control; BG5 periodic), and $n = 8$ (S24 random and periodic) from 2 biologically independent experiments; Mixed-effects analysis, Holm-Šidák test. **g, j–p**, Data are presented as mean values \pm s.e.m. ns, not significant ($P \geq 0.05$).



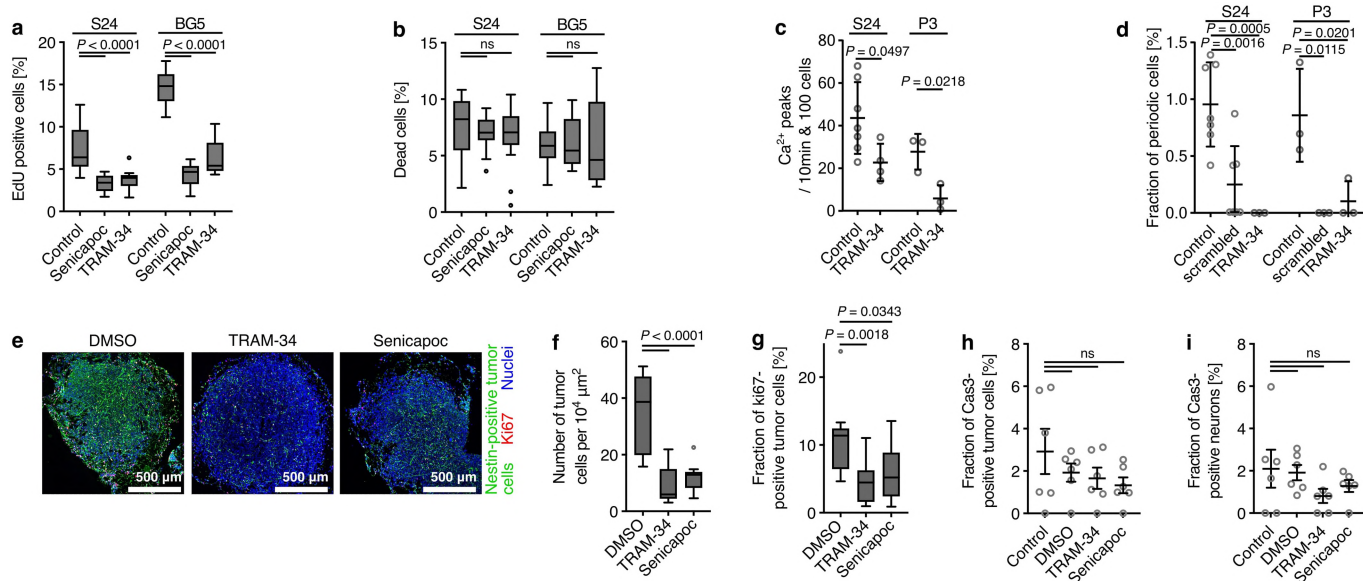
Extended Data Fig. 3 | Tumor cell networks have scale-free and small-world properties, and their functional network hubs frequently display periodic calcium oscillations *in vivo* and *in vitro*. **a–c**, Mean probability distribution of coactive cells per cell from *in vitro* and *in vivo* Ca²⁺ imaging plotted in a log-log scale with linear regression fit in red and the fitted random Poisson distribution in green; the grey box indicates highly connected network hubs; Pearson correlation. **d**, $\langle k \rangle$ (mean number of connections per cell) and σ (standard deviation of number of connections per cell) of all recorded networks from each condition. For a random network with Poisson degree distribution the standard deviation of the degrees follows $\sigma = \langle k \rangle^{1/2}$ shown as a red dashed line on the figure. For each network σ is larger than the value expected for a random network with the same $\langle k \rangle$, which leads to the manifestation of scale-free properties in the

networks⁷. **e–h**, Network parameters λ (mean shortest path length) and σ (clustering coefficient) calculated for recorded networks and their corresponding Erdős-Rényi random networks of equal number of nodes and edges; error bars show s.e.m.; paired two-sided t-test. **a–h**, $n = 24$ recordings from 3 mice (S24 *in vivo*), $n = 22$ recordings from 9 biologically independent experiments (S24 *in vitro*), $n = 40$ recordings from 4 mice (BG5 *in vivo*), and $n = 10$ recordings from 5 biologically independent experiments (BG5 *in vitro*). **i–n**, Network plot of cross-correlation coefficients larger than cut-off derived from the same Ca²⁺ recordings of tumor cells; BG5 line *in vitro* (**i**, **l**); S24 line *in vivo* (**j**, **m**); BG5 line *in vivo* (**k**, **n**); scale bars are 100 μ m (**i**) and 50 μ m (**j**, **k**). **o–q**, Ca²⁺ transients of indicated TM-connected tumor cells; dark red transients originated from a periodic cell. ns, not significant ($P \geq 0.05$).



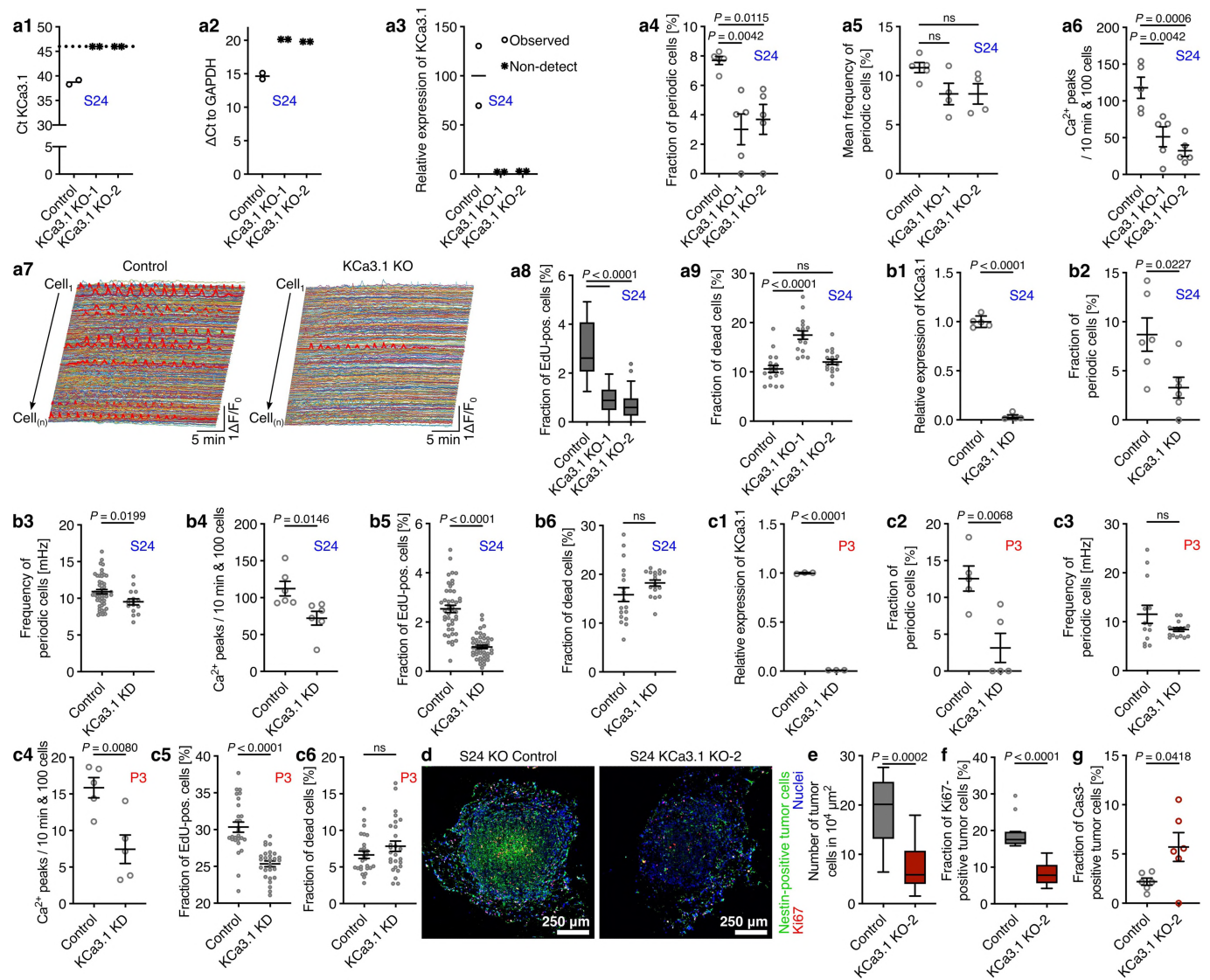
Extended Data Fig. 4 | Ablation of periodically active cells reduces network integrity. **a**, Fraction of periodic cells of all active cells and all network hubs in experimental data *in vivo* and all cells in scrambled data; $n = 24$ recordings from 3 mice (S24) and $n = 40$ recordings from 4 mice (BG5); error bars show s.e.m.; Mixed-effects analysis, Dunnett's test. **b**, Venn diagram of active cells, communicating cells, periodic cells, and functional network hubs; periodic cells are solely defined by their low peak-peak-interval variability (bright red) and convey their effect on the network by often being highly connected network hubs (dark red). **c**, Number of ablated periodic cells and randomly chosen active cells per FOV *in vitro* (comparable in both groups); $n = 6$ recordings (BG5 control and random), $n = 7$ (S24 control; BG5 periodic), and $n = 8$ (S24 random and periodic) from 2 biologically independent experiments; two-sided t-test. **d**, Fraction of activated caspase-3-positive cells (i.e., cells undergoing apoptosis) in ablated and non-ablated cells; all ablated cells were apoptotic; $n = 6$ recordings per group from 2 biologically independent experiments; two-sided t-test.

e–g, Global Ca^{2+} activity and number of communicating cells per FOV of Ca^{2+} recordings *in vitro* before and 1 h after cell-specific laser ablation of either no cells (control), all periodic cells, or the corresponding number of randomly chosen active cells; BG5 line, $n = 6$ recordings (control and random ablation) and $n = 7$ recordings (ablation of periodic cells) in 2 biologically independent experiments (e); S24 line, $n = 7$ recordings (control) and $n = 8$ recordings (random and periodic) in 2 biologically independent experiments (f,g); one-way ANOVA, Dunnett's test. **h**, Fraction of dead cells, measured as number of PI-positive cells (dead cells) divided by DAPI-positive cells (nuclei), 24 h after the cell-specific laser ablation of either periodic cells (periodic), the corresponding number randomly chosen active cells (random), or no cells (control); S24 line; $n = 6$ recordings per group from 2 biologically independent experiments; Kruskal-Wallis test, Dunn's test. **c–h**, Error bars show s.d. ns, not significant ($P \geq 0.05$).



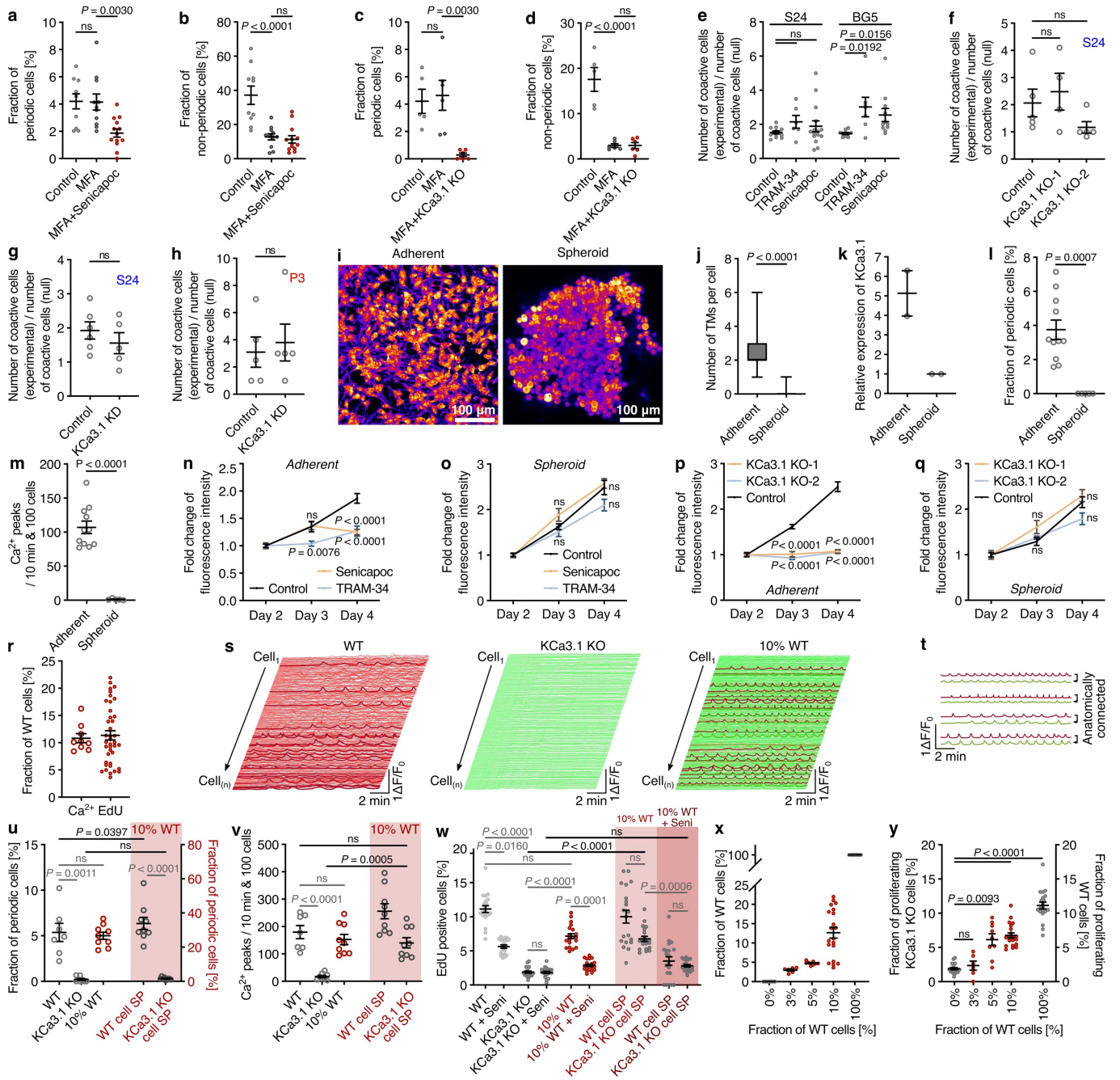
Extended Data Fig. 5 | KCa3.1 inhibition reduces tumor cell proliferation *in vitro* and in human cerebral brain organoids. **a**, Fraction of EdU-positive cells after control versus 1 μ M TRAM-34 and 1 μ M Senicapoc treatment *in vitro*; n = 18 FOVs from 2 biologically independent experiments for each group; one-way ANOVA, Dunnett's test. **b**, Fraction of dead cells, measured as number of PI-positive cells divided by DAPI-positive cells in control versus TRAM-34 and Senicapoc treatment *in vitro*; n = 18 FOVs from 2 biologically independent experiments for each group; one-way ANOVA, Dunnett's test. **c**, Global Ca^{2+} activity and **d**, fraction of periodic cells of all active cells in control versus TRAM-34 (10 μ M) treatment in a human cerebral organoid glioma model; patient-derived human glioblastoma cell lines S24 and P3; n = 7 recordings (S24, control) from 4 organoids, n = 4 recordings (S24, TRAM-34) from

2 organoids, and n = 3 recordings (P3, control and TRAM-34) from 2 organoids, respectively; one-way ANOVA, Dunnett's test. **e**, Representative immunofluorescence images, **f**, tumor cell density and **g**, fraction of Ki67-positive tumor cells in tumor-bearing human cerebral organoids after 14 days of control versus 1 μ M TRAM-34 or 1 μ M Senicapoc treatment; n = 12 regions in 6 human cerebral organoids per group; S24 line; one-way ANOVA, Dunnett's test (**f**) and Kruskal-Wallis test, Dunn's test (**g**). **h**, and **i**, Fraction of activated caspase-3-positive tumor cells (**h**) and neurons (**i**) in tumor-bearing human cerebral organoids after 14 days of no treatment (control), DMSO control, TRAM-34 and Senicapoc treatment; n = 6 regions in 3 organoids per group; S24 line; one-way ANOVA, Dunnett's test (**h**) and Kruskal-Wallis test, Dunn's test (**i**). Error bars show s.e.m. ns, not significant ($P \geq 0.05$).



Extended Data Fig. 6 | Genetic perturbation of KCa3.1 reduces intrinsic rhythmicity, global Ca^{2+} activity, and tumor cell proliferation. **a**, KCa3.1 knockout (KO; 2 different sgRNAs) versus knockout control (non-targeting sgRNA); S24 line. For both KOs no KCa3.1 signal was detected. Therefore, the qPCR cycle limit +1 was used as the hypothetical timepoint of detection for quantifying the relative KO of KCa3.1. **b**, KCa3.1 knockdown (KD) versus knockdown control (non-targeting shRNA); S24 line. **c**, KCa3.1 knockdown (KD) versus knockdown control (non-targeting shRNA); P3 line. **a1-3**, **b1**, and **c1**, Relative expression of KCa3.1 as determined *via* qPCR; $n = 2$ technical replicates (S24 KO control, S24 KCa3.1 KO-1 & -2), $n = 5$ technical replicates from 2 biologically independent experiments (S24 KD control, S24 KCa3.1 KD), $n = 3$ technical replicates (P3 KD control, P3 KCa3.1 KD). **a4**, **b2**, and **c2**, Fractions of periodic cells of all active cells *in vitro*. **a5**, **b3**, and **c3**, Frequencies of Ca^{2+} oscillations of periodic cells *in vitro*. Note that the difference between the groups in **b3** reaches statistical significance but is minor, and thus of questionable biological relevance. **a6**, **b4**, and **c4**, Global Ca^{2+} activity *in vitro*. **a7**, Ca^{2+} traces of each cell from representative recordings; dark red: periodic cells. **a8**, **b5**, and **c5**, Fraction of EdU-positive cells *in vitro*. **a9**, **b6**, and **c6**,

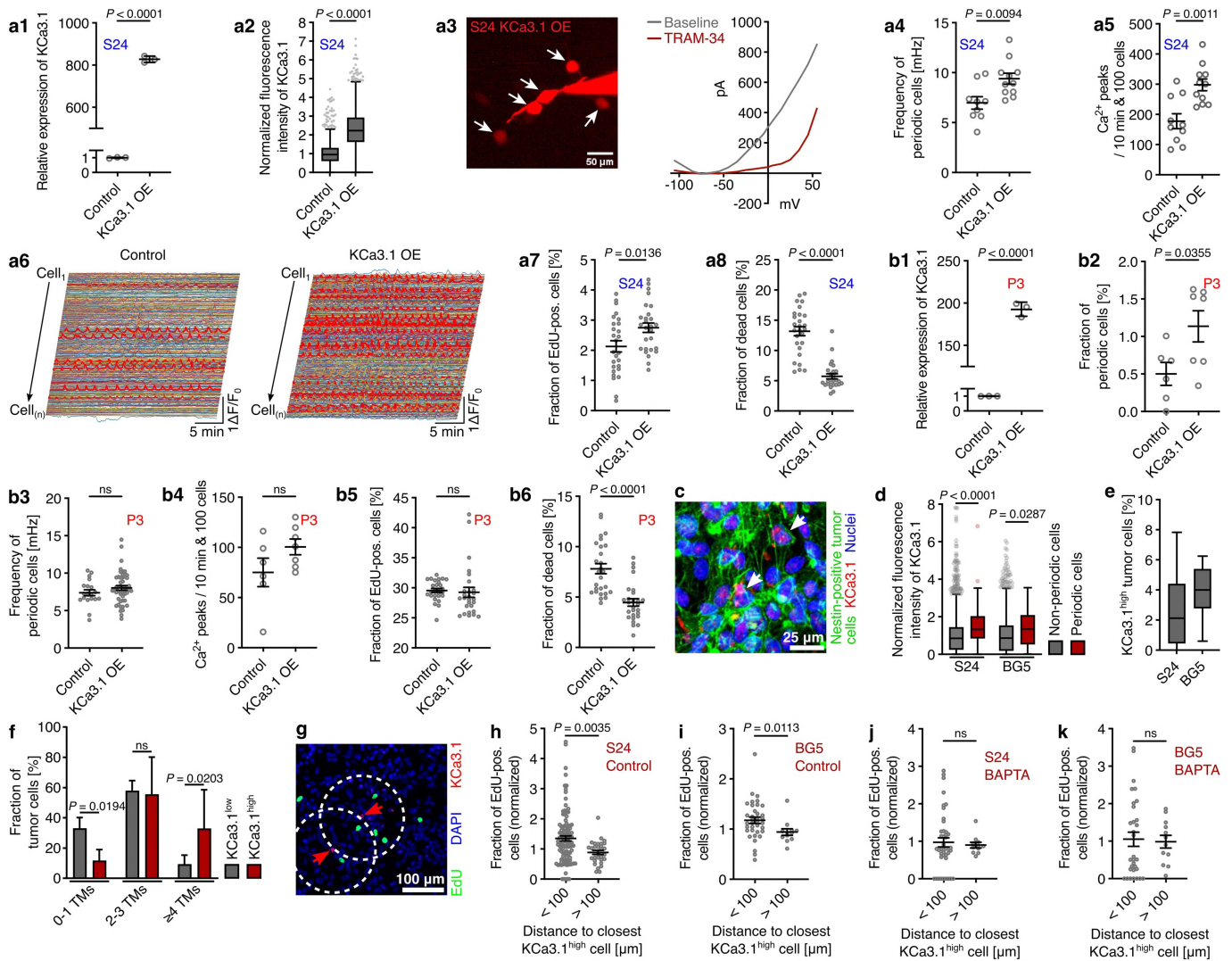
Fractions of dead cells *in vitro*. **a4-6**, **b2-4**, and **c2-4**, $n = 5$ recordings (S24 KO control, S24 KCa3.1 KO-1 & -2), $n = 6$ recordings (S24 KD control and S24 KCa3.1 KD), $n = 5$ recordings (P3 KD control and P3 KCa3.1 KD) from 2 biologically independent experiments per group, respectively. **a8-9**, **b5-6**, and **c5-6**, $n = 27$ FOVs (S24 KO control (EdU) and S24 KCa3.1 KO-1 & -2 (EdU)), $n = 18$ FOVs (S24 KO control (dead cells) and S24 KCa3.1 KO-1 & -2 (dead cells)), $n = 45$ FOVs (S24 KD control (EdU) and S24 KCa3.1 KD (EdU)), $n = 18$ FOVs (S24 KD control (dead cells) and S24 KCa3.1 KD (dead cells)), $n = 27$ FOVs (P3 KD control and P3 KCa3.1 KD) from 2 biologically independent experiments per group, respectively. **a4-6**, **a8**, One-way ANOVA, Dunnett's test. **a9**, Kruskal-Wallis test, Dunn's test. **b1-6**, **c1-2**, and **c4**, two-sided t-test. **c3**, and **c5-6**, two-sided Mann-Whitney test. **d**, Representative immunofluorescence images, **e**, tumor cell density **f**, fraction of Ki67-positive tumor cells, and **g**, fraction of activated caspase-3-positive tumor cells of tumor-bearing cerebral human organoids after implantation of S24 KO control and S24 KCa3.1 KO-2 line; $n = 12$ regions in 6 human cerebral organoids per group (**e**, **f**) and $n = 6$ regions in 3 human cerebral organoids per group (**g**); two-sided t-test (**e**, **g**) and two-sided Mann-Whitney test (**f**). Error bars show s.e.m. ns, not significant ($P \geq 0.05$).



Extended Data Fig. 7 | See next page for caption.

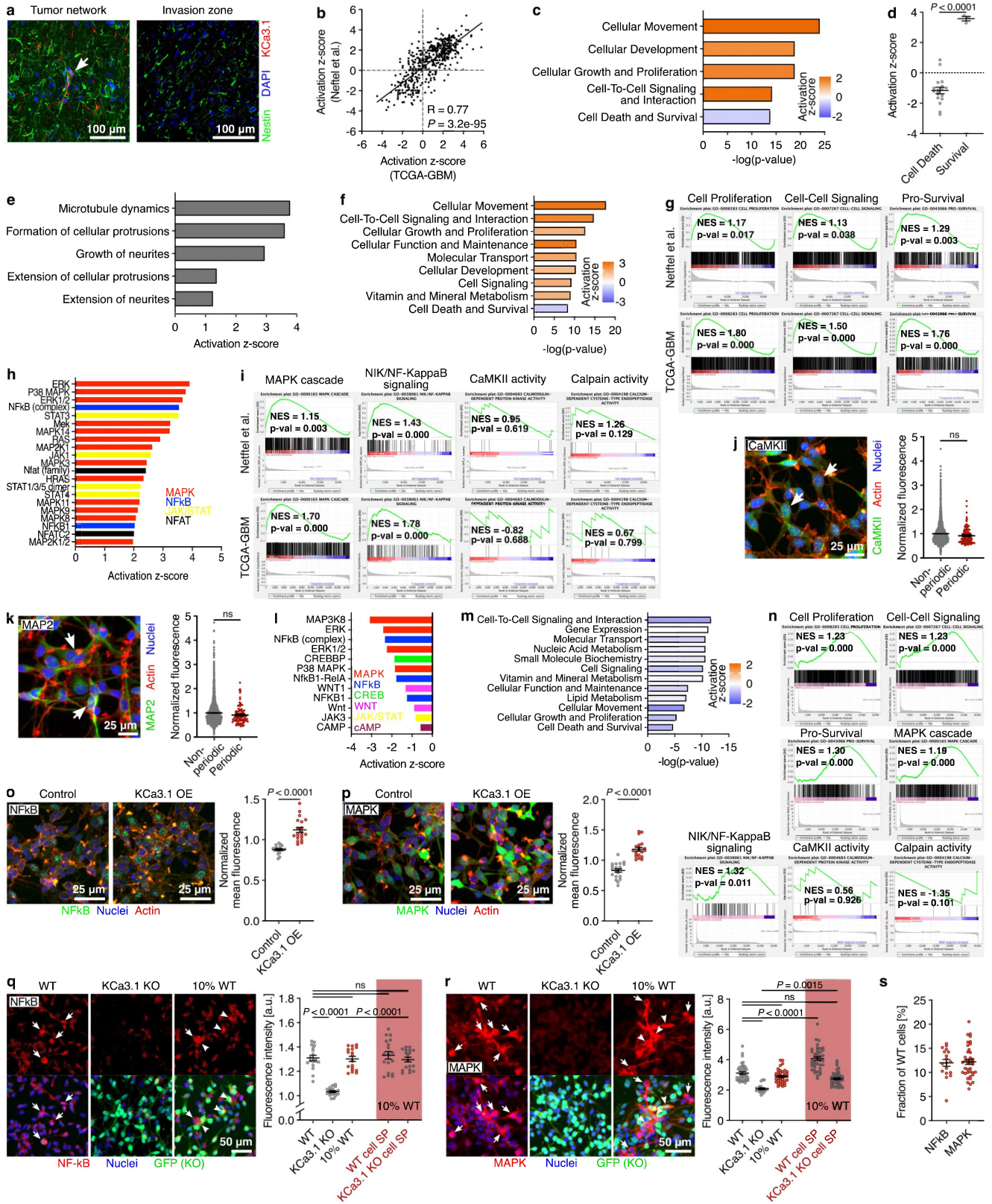
Extended Data Fig. 7 | KCa3.1 drives periodic Ca^{2+} oscillations and their proliferation-stimulating effects in glioblastoma cell networks. a–d. After gap junction inhibition *via* MFA, pharmacological inhibition, and genetic perturbation of KCa3.1 strongly reduce the fraction of cells displaying periodic Ca^{2+} activity but do not affect the remaining sporadic non-periodic Ca^{2+} activity, demonstrating a specific effect on periodic Ca^{2+} activity that – due to gap junction inhibition – is unlikely to be mediated by nonspecific effects on global Ca^{2+} communication. **a,b.** Fraction of cells displaying periodic (**a**) and non-periodic (**b**) Ca^{2+} activity of all cells after treatment with 100 μ M MFA and with both MFA and 1 μ M Senicapoc *in vitro*; S24 line; n = 10 recordings (Control), n = 11 recordings (MFA), and n = 13 recordings (MFA+Senicapoc) from 2 biologically independent experiments, respectively; One-way ANOVA, Dunnett’s test. **c,d.** Fraction of cells displaying periodic (**c**) and non-periodic (**d**) Ca^{2+} activity after treatment with MFA and after both genetic knockout of KCa3.1 and treatment with MFA *in vitro*; n = 5 recordings (S24 KO control line, no treatment; “Control”), n = 6 recordings (S24 KO control line, MFA treatment; “MFA”), and n = 6 recordings (S24 KCa3.1 KO-2 line, MFA treatment; “MFA+KCa3.1 KO”) from 2 biologically independent experiments, respectively; One-way ANOVA, Dunnett’s test. **e–h.** Intercellular coactivity is not reduced in Ca^{2+} recordings of control versus 1 μ M TRAM-34 and 1 μ M Senicapoc treatment (**e**), S24 KO control versus S24 KCa3.1 KO-1 and KO-2 (**f**), S24 KD control versus S24 KCa3.1 KD (**g**), and P3 control versus P3 KCa3.1 KD (**h**) *in vitro*; intercellular coactivity was calculated by dividing the number of coactive cells of a recording by the number of coactive cells of its corresponding null control data, representing the overall degree to which active cells are communicating their Ca^{2+} activity to other cells; increased intercellular coactivity after KCa3.1 inhibitor treatment might be because the strongly reduced number of periodic cells leads to less interference of different signals and therefore an even stronger synchronization between cell pairs. **e**, n = 11 recordings (S24, control treatment), n = 6 recordings (S24, TRAM-34), n = 15 recordings (S24, Senicapoc), n = 10 recordings (BG5, control treatment), n = 7 recordings (BG5, TRAM-34), and n = 11 recordings (BG5, Senicapoc) from 2 biologically independent experiments; Kruskal-Wallis test, Dunn’s test. **f–h**, n = 5 recordings (S24 KO control, S24 KCa3.1 KO-2), n = 4 recordings (S24 KCa3.1 KO-1), n = 6 recordings (S24 KD control), n = 5 recordings (S24 KCa3.1 KD), and n = 5 recordings (P3 KD control, P3 KCa3.1 KD) from 2 biologically independent experiments per group, respectively. **f**, One-way ANOVA, Dunnett’s test; **g**, two-sided t-test; **h**, two-sided Mann-Whitney test. **i.** Representative images of cells in adherent and spheroid conditions; in spheroid conditions tumor cells do not form networks (**j**) and do not display periodic activity (**l**), resulting in a much lower KCa3.1 expression (**k**), and therefore also do not show any Ca^{2+} activity (**m**). **j.** Number of TMs per cell in adherent versus spheroid conditions; n = 45 cells from 3 recordings from 3 biologically independent experiments (adherent) and n = 1087 cells from 5 recordings from 2 biologically independent experiments (spheroid); two-sided Mann-Whitney test. **k.** Relative expression of KCa3.1 in adherent versus spheroid conditions as determined via qPCR; n = 2 technical replicates; two-sided t-test. **l.** Fraction of periodic cells and **m.** global Ca^{2+} activity in adherent versus spheroid conditions; n = 11 recordings from 3 biologically independent

experiments (adherent) and n = 5 recordings from 2 biologically independent experiments (spheroid); S24 line; two-sided t-test. **n–q.** AlamarBlue proliferation assay demonstrates that specific KCa3.1 inhibition with 1 μ M TRAM-34 and 1 μ M Senicapoc and genetic knockout of KCa3.1 reduces proliferation in adherent conditions (**n,p**) but not in spheroid conditions (**o,q**); S24 line; n = 12 measurements per group from 2 biologically independent experiments; one-way ANOVA, Dunnett’s test. **r.** Fraction of wild-type (WT) cells of all cells in Ca^{2+} recordings (Ca^{2+}) displayed in Fig. 4c–f and Extended Data Fig. 7u,v and in recordings of the EdU proliferation assay (EdU) displayed in Fig. 4g–i and Extended Data Fig. 7w after coculturing S24 wild-type cells with S24 KCa3.1 KO-2 cells; n = 9 recordings (Ca^{2+}) and n = 40 recordings (EdU) in 2 biological independent experiments, respectively. **s.** Ca^{2+} traces from representative recordings of S24 wild-type cells (WT), S24 KCa3.1 KO-2 cells and of a co-culture of 10% S24 wild-type cells with S24 KCa3.1 KO-2 cells (10% WT); traces of wild-type cells are depicted in red, traces of KCa3.1 knockout cells are depicted in green, and traces of cells displaying periodic Ca^{2+} activity are depicted thicker and darker; adding wild-type cells rescues the effect of the KCa3.1 knockout on global Ca^{2+} activity. **t.** Rarely detected periodic activity in knockout cells (green) after cocultivation with wild-type cells is due to close cupelling with periodically active wild-type cells (red); representative Ca^{2+} traces from **s**. **u–w.** Same data as shown in Fig. 4c–i, which originates from joint experiments with multiple experimental groups, and is shown here in one instead of two graphs to allow statistical comparison between the subpopulations (SP) of the co-culture and the control conditions (WT and KCa3.1 KO). Black p-values indicate these comparisons and grey p-values indicate comparisons that are also depicted in the respective main figure (Fig. 4c–i). P-values can differ here due to multiple testing; **u.** Fraction of periodic cells of all cells, **v.** global Ca^{2+} activity, and **w.** fraction of EdU-positive cells in recordings of S24 wild-type cells (WT), of S24 KCa3.1 KO-2 cells, of a co-culture of 10% S24 wild-type cells with S24 KCa3.1 KO-2 cells (10% WT) and of the subpopulations (SP) of S24 wild-type cells and S24 KCa3.1 KO-2 cells in the respective co-culture. **u,v**, n = 7 recordings (WT), n = 8 recordings (KCa3.1 KO), and n = 9 recordings (Co-culture) in 2 biological independent experiments; one-way ANOVA, Dunnett’s test (**u**) and Kruskal-Wallis test, Dunn’s test (**v**). **w**, n = 20 recordings in 2 biological independent experiments for all groups respectively; Kruskal-Wallis test, Dunn’s test. **x.** Fraction of wild-type (WT) cells and **y.** fraction of EdU-positive cells in recordings of S24 wild-type cells (100%), S24 KCa3.1 KO-2 cells (0%) and of a co-culture of 3, 5 and 10% S24 wild-type cells with S24 KCa3.1 KO-2 cells; **y**, for 0, 3, 5, an 10% WT cells the fraction of proliferating KO cells is shown on the left y-axis, for comparison the fraction of proliferating cells in WT-monoculture (100%) is shown on the right y-axis. While the co-culture of 5% WT cells still significantly increases the proliferation of the KCa3.1 KO, the co-culture of 3% of WT cells does not, placing the lower limit of WT cells to rescue the effects of the KCa3.1 KO somewhere between 3–5%. Kruskal-Wallis test, Dunn’s test. **x,y**, n = 20 recordings (0%, 10%, 100%), n = 6 recordings (3%), and n = 9 recordings (5%), in 2 biological independent experiments for all groups. Error bars show s.e.m. ns, not significant ($P \geq 0.05$).



Extended Data Fig. 8 | Tumor biological effects of KCa3.1 overexpression, and further *in vitro* characterizations. **a**, KCa3.1 overexpression (OE) versus control; S24 line. **b**, KCa3.1 overexpression (OE) versus control; P3 line. **a1** and **b1**, Relative expression of KCa3.1 as determined *via* qPCR; n = 3 technical replicates. **a2**, Normalized KCa3.1 immunofluorescence values of all cells (see Methods for more details). **a3**, Whole-cell patch-clamp electrophysiology of S24 cells overexpressing KCa3.1; arrows indicate glioblastoma cells connected *via* gap junctions filled *via* the patch pipette containing Alexa 594 dye; on the right side, I-V curves of voltage ramps between -105 mV to 55 mV are shown before (grey trace) and after wash-in of 1 μ M TRAM-34 (red trace). TRAM-34 sensitive currents were detected in all S24 KCa3.1 overexpression cells (n = 4 cells), but in none of the control S24 cells (n = 3 cells). **b2**, Fraction of periodic cells of all active cells *in vitro*. **a4**, and **b3**, Frequency of Ca²⁺ oscillation of periodic cells *in vitro*. **a5** and **b4**, Global Ca²⁺ activity *in vitro*. **a6**, Ca²⁺ traces of each cell from representative recordings; dark red: periodic cells. **a7** and **b5**, Fraction of EdU-positive cells *in vitro*. **a8**, and **b6**, Fraction of dead cells *in vitro*. **a2**, n = 1810 cells (S24 OE control) and n = 1532 cells (S24 KCa3.1 OE) from 6 FOVs, respectively; **a4**–**5**, and **b2**–**4**, n = 10 recordings (S24 OE control), n = 11 recordings (S24 KCa3.1 OE), n = 6 recordings (P3 OE control), n = 7 recordings (P3 KCa3.1 OE) from 2 biologically independent experiments per group, respectively. **a7**–**8**, and **b5**–**6**, n = 27 FOVs from 2 biologically independent experiments per group, respectively. **a1**, **a4**–**8**, **b1**–**2**, and **b4**, two-sided t-test. **a2**, **b3**, and **b5**–**6**, two-sided Mann-Whitney test. **c**, Representative Nestin and KCa3.1 double-immunostaining after Ca²⁺ recordings of the same region *in vitro*; arrows indicate cells that displayed periodic Ca²⁺ oscillations in the

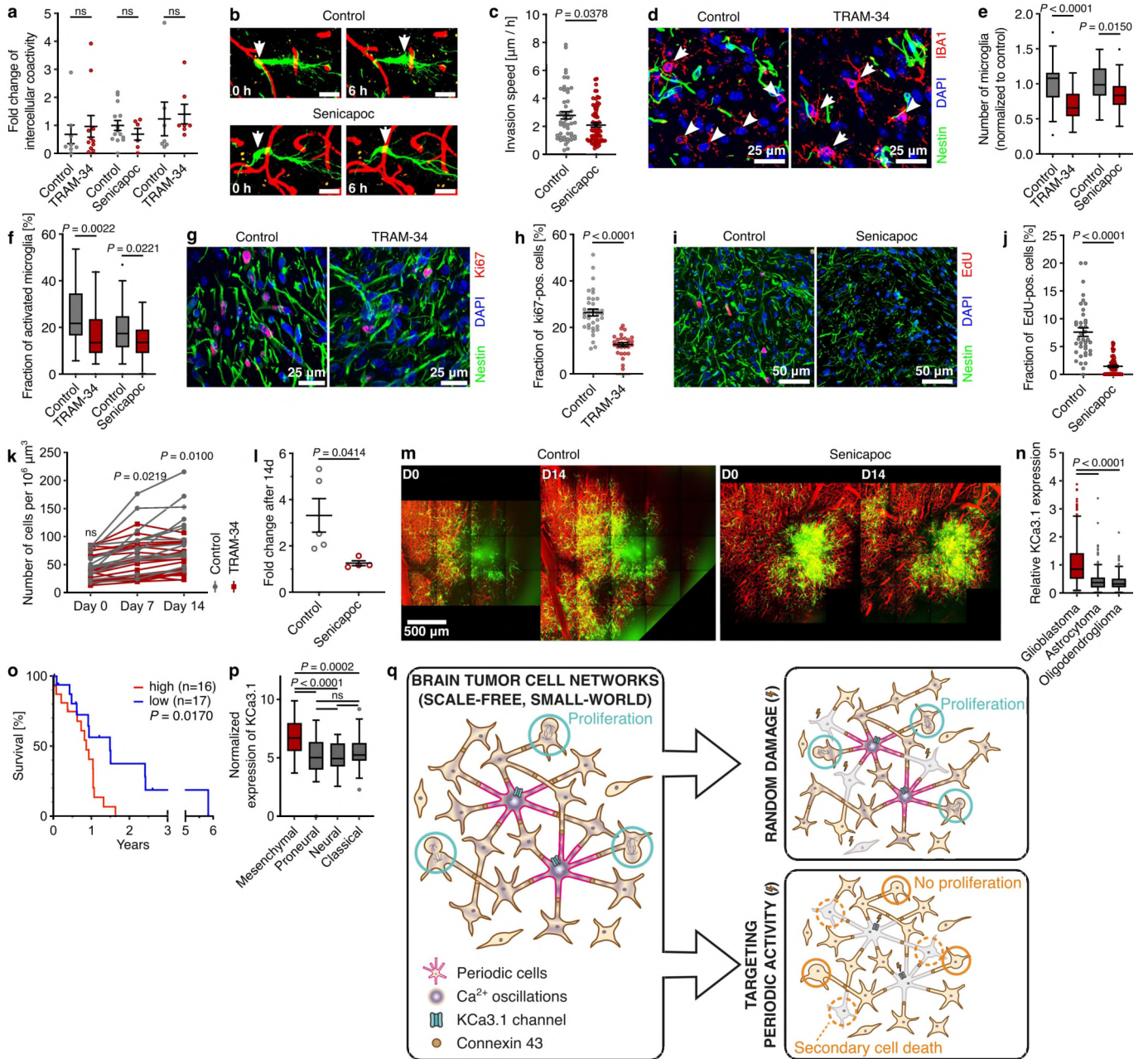
preceding Ca²⁺ recording; S24 line. **d**, Normalized KCa3.1 immunofluorescence values after calcium recordings in periodic cells and non-periodic cells (see Methods for more details); periodic cells show a 51.1% \pm 11.1% (95% CI) for S24 and 43.2% \pm 17.0% (95% CI) for BG5 higher fluorescence intensity than non-periodic cells. **c**, **d**, n = 3177 S24 non-periodic cells, n = 75 S24 periodic cells, n = 3108 BG5 non-periodic cells, and n = 29 BG5 periodic cells from n = 5 recordings per cell line from n = 3 biologically independent experiments; Kruskal-Wallis test, Dunn's test. **e**, fraction of KCa3.1^{high} tumor cells growing in mice; n = 27 regions in 4 mice (S24 line) and n = 21 regions in 3 mice (BG5 line). **f**, Fraction of tumor cells with the respective number of TMs per tumor cell in KCa3.1^{high} and KCa3.1^{low} cells; immunostainings of tumors growing in mice; error bars show s.d.; S24 line; n = 12 regions in 3 mice; Kruskal-Wallis test, Dunn's test. **g**, Representative KCa3.1 and EdU immunostainings of S24 line; arrows indicate the KCa3.1^{high} cells; dashed circles indicate the radius of 100 μ m around the KCa3.1^{high} cells; n = 18 recordings from 2 biologically independent experiments. **h**–**k**, Fraction of EdU-positive cells with a distance < 100 μ m versus > 100 μ m to the closest KCa3.1^{high} cell normalized to the fraction of EdU-positive cells of each recording; **h**, S24 line control conditions, n = 106 ROIs (<100 μ m) and n = 30 (>100 μ m) in 2 biologically independent experiments, **i**, BG5 line control conditions, n = 36 ROIs (<100 μ m) and n = 12 (>100 μ m) in 2 biologically independent experiments, **j**, S24 line BAPTA-AM treatment, n = 42 ROIs (<100 μ m) and n = 11 (>100 μ m) in 2 biologically independent experiments, and **k**, BG5 line BAPTA-AM treatment, n = 31 ROIs (<100 μ m) and n = 12 (>100 μ m) in 2 biologically independent experiments; two-sided Mann-Whitney test. Error bars show s.e.m. ns, not significant (P \geq 0.05).



Extended Data Fig. 9 | See next page for caption.

Extended Data Fig. 9 | KCa3.1 expression is associated with distinct molecular features in glioblastoma. **a**, Double-immunofluorescence of Nestin and KCa3.1 in a human glioblastoma sample of a representative tumor network region and invasion zone; arrow indicates KCa3.1^{high} tumor cell; n = 30 ROIs (tumor network) and n = 30 ROIs (invasion zone) in 3 samples from different patients. **b**, Ingenuity Pathway Analysis (IPA) was performed using the differential gene expression of KCa3.1^{high} versus KCa3.1^{low} cells in a scRNA-seq dataset of 28 glioblastoma by Neftel et al.³⁸, and the differential gene expression of the top versus the bottom quartile of KCa3.1 expressing TCGA-GBM glioblastoma (n = 36 patients (top) and 37 patients (bottom)); scatter plot and simple linear regression with f-test of all activation z-scores of the upstream regulator analysis by IPA reveals accordance between both datasets; n = 621 upstream regulators. **c–e**, Ingenuity Pathway Analysis (IPA) using the differential gene expression of KCa3.1^{high} versus KCa3.1^{low} cells in a scRNA-seq dataset of 28 glioblastoma by Neftel et al.³⁸. **c**, Top differentially regulated molecular and cellular functions; the respective activation z-score is color-coded as indicated (higher values (orange) represent an upregulation in KCa3.1^{high} cells and lower values (blue) a downregulation); right-tailed Fisher's exact test. **d,e**, Box plot showing the activation z-scores of all differentially regulated molecular and cellular functions associated with cell death and survival (**d**) and growth of protrusions (**e**); n = 18 (death) and n = 3 (survival); two-sided t-test; error bars show s.e.m. **f,h**, Ingenuity Pathway Analysis (IPA) was performed using the differential gene expression of the top versus the bottom quartile of KCa3.1 expressing TCGA glioblastoma (n = 36 patients (top) and 37 patients (bottom)). **f**, Top differentially regulated molecular and cellular functions; the respective activation z-score is color-coded as indicated; right-tailed Fisher's exact test. **h**, Activation z-scores of the top activated signaling pathways. **g,i**, Using the differential gene expression of KCa3.1^{high} versus KCa3.1^{low} cells in the scRNA-seq dataset of 28 glioblastoma by Neftel et al.³⁸, and the differential gene expression of the top versus the bottom quartile of KCa3.1 expressing TCGA-GBM glioblastoma (n = 36 patients (top) and 37 patients (bottom)) a gene set expression analysis (GSEA) of the GO-Terms "cell proliferation", "cell-cell signaling", "pro-survival", "MAPK cascade", "NIK/NF-KAPPAB signaling", "calcium-dependent cysteine-type endopeptidase activity", and "calmodulin-dependent protein kinase activity" was performed. **j**, Representative phospho-CaMKII (Thr286) and **k**, MAP2 immunofluorescence images and immunofluorescence values; arrows indicate cells that displayed periodic Ca²⁺ oscillations in the preceding Ca²⁺ recording; Calpain translates high-frequency

Ca²⁺ transients into decomposition of its sensitive substrate, MAP2²⁸. The MAP2 fluorescence intensity therefore correlates inversely with the Calpain activity; S24 line; n = 3069 cells (non-periodic, CaMKII), n = 114 (periodic, CaMKII), n = 3279 cells (non-periodic, MAP2), and n = 102 (periodic, MAP2) from 8 recordings from 2 biologically independent experiments, respectively; two-sided Mann-Whitney test. **l,m**, Ingenuity Pathway Analysis (IPA) was performed using the differential gene expression after control versus KCa3.1 inhibition *in vitro* using Senicapoc; right-tailed Fisher's exact test. **l**, Activation z-score of top downregulated signaling pathways. **m**, Top differentially regulated molecular and cellular functions; the respective activation z-score is color-coded as indicated. **n**, Using the differential gene expression after control versus KCa3.1 inhibition *in vitro* using Senicapoc a gene set expression analysis (GSEA) of the GO-Terms "cell proliferation", "cell-cell signaling", "pro-survival", "MAPK cascade", "NIK/NF-KAPPAB signaling", "calcium-dependent cysteine-type endopeptidase activity", and "calmodulin-dependent protein kinase activity" was performed. **o**, Representative phospho-NF-κB and **p**, phospho-p44/42 MAPK immunofluorescence images and normalized mean immunofluorescence values of all cells in the FOV *in vitro*, S24 KCa3.1 overexpression (KCa3.1 OE) versus S24 OE control (Control); n = 20 FOVs (KCa3.1 OE) and n = 20 FOVs (Control) from 2 biologically independent experiments, respectively; two-sided t-test. **q,r**, Coculturing 10% wild-type cells with KCa3.1 knockout cells rescues the suppressive effect of the KCa3.1 KO on NF-κB and p44/42 MAPK activity. Representative phospho-NF-κB (**q**) and phospho-p44/42 MAPK (**r**) immunofluorescence images and normalized mean immunofluorescence values of all cells in the FOV *in vitro*; data is shown for S24 wild-type cells (WT), for S24 KCa3.1 KO-2 cells, for a co-culture of 10% S24 wild-type cells with S24 KCa3.1 KO-2 cells (10% WT) and for the subpopulation (SP) of S24 wild-type cells and S24 KCa3.1 KO-2 cells in the respective co-culture; NF-κB: n = 18 recordings from 2 biologically independent experiments for all conditions, respectively, one-way ANOVA, Dunnett's test; p44/42 MAPK: n = 39 FOVs (WT & 10% WT) and n = 20 FOVs (KCa3.1 KO) from 2 biologically independent experiments, respectively, Kruskal-Wallis test, Dunn's test. **s**, Fraction of wild-type (WT) cells of all cells in recordings of the immunocytochemistry of the NF-κB- and MAPK-pathways displayed in **q** and **r** after coculturing S24 wild-type cells with S24 KCa3.1 KO-2 cells; n = 18 recordings (NFκB) and n = 39 recordings (MAPK) in 2 biological independent experiments, respectively. Error bars show s.e.m.



Extended Data Fig. 10 | See next page for caption.

Extended Data Fig. 10 | Relevance of KCa3.1 functionality for brain tumor progression. **a**, Fold change of intercellular coactivity in Ca^{2+} recordings from control and either TRAM-34 (i.p., 120 mg/kg) or Senicapoc (i.p., 50 mg/kg) treated mice; intercellular coactivity was calculated by dividing the number of coactive cells of a recording by the number of coactive cells of its corresponding null control data; KCa3.1 inhibition did not hinder cell-to-cell signaling as such, ruling out that the reduced global Ca^{2+} activity (Fig. 6b) is solely due to nonspecifically altered Ca^{2+} dynamics; n = 8 and 11 recordings in 4 mice for control and TRAM-34 treatments, respectively in S24, n = 14 and 6 recordings in 4 mice for control and Senicapoc treatments, respectively in S24, n = 7 recordings in 4 and 3 mice for control and TRAM-34 treatments in BG5, respectively; Kruskal-Wallis test, Dunn's test. **b**, Representative time series of tumor cells (green) and brain microvessels (red) under control conditions versus Senicapoc treatment; arrows indicate somata of tumor cells; scale bars are 25 μm . **c**, Invasion speed of tumor cells; BG5 line. **b, c**, n = 49 cells under control conditions in 4 mice and n = 71 cells under Senicapoc treatment in 4 mice; Mann Whitney test. **d**, Representative immunofluorescence staining of Nestin (tumor cells) and IBA1 (microglia) in patient-derived human glioblastoma xenografts (S24 line) in mouse brains after TRAM-34 treatment (2x 120 mg/kg per day) versus control; arrowheads show activated microglia and arrows show surveilling microglia according to morphological criteria (see Methods for more details). **e**, Number of microglia and **f**, fraction of activated microglia in patient-derived human glioblastoma xenografts in mouse brains after TRAM-34 treatment (2x 120 mg/kg per day) and Senicapoc treatment (2x 50 mg/kg per day) versus control. **d-f**, n = 31 FOVs in 5 mice for control and n = 38 FOVs in 3 mice for TRAM-34; n = 48 FOVs in 4 mice for control and n = 61 FOVs in 4 mice for Senicapoc; Kruskal-Wallis test, Dunn's test. **g**, Representative immunofluorescence stainings for Nestin and Ki67 and **h**, fraction of Ki67-positive tumor cells in patient-derived

human glioblastoma xenografts (S24 line) in mouse brains after TRAM-34 treatment (2x 120 mg/kg per day) versus control; n = 36 FOVs in 5 mice for control and n = 28 FOVs in 3 mice for TRAM-34; two-sided Mann-Whitney test. **i**, Representative immunofluorescence staining of Nestin and EdU and **j**, fraction of EdU-positive tumor cells in patient-derived human glioblastoma xenografts (BG5 line) in mouse brains after Senicapoc treatment (2x 50 mg/kg per day) versus vehicle control and *in vivo* EdU incorporation; n = 39 FOVs in 4 mice for control and n = 64 FOVs in 4 mice for Senicapoc; two-sided Mann-Whitney test. **k**, Change in tumor cell density on day 14 versus day 0 under control conditions versus TRAM-34 treatment (2x 120 mg/kg per day); n = 14 regions in 4 mice (control) and n = 21 regions in 4 mice (TRAM-34); Kruskal-Wallis test, Dunn's test. **l**, Number of tumor cells and **m**, representative tile-scan images of tumors (green) and brain vessels (red) on day 14 versus day 0 under control versus Senicapoc treatment (2x 50 mg/kg per day); BG5 line; n = 5 mice for control conditions and n = 4 mice for Senicapoc treatment; two-sided t-test. **n**, KCa3.1 expression values ($\log_2(\text{FPKM} + 1)$) in glioblastoma (n = 230 patients), IDH-mutant and 1p/19q intact lower grade glioma (n = 241 patients), and IDH-mutant and 1p/19q codeleted oligodendroglioma (n = 176 patients) from TCGA datasets; Kruskal-Wallis test, Dunn's test. **o**, Kaplan-Meier survival plot of glioblastoma patients of the mesenchymal gene expression subtype with the highest versus lowest third of KCa3.1 expression; the significant difference between groups indicates that the prognostic effect of KCa3.1 is not simply due to its correlation with mesenchymal tumors, which have been associated with a worse prognosis⁷⁰; log-rank test. **p**, Normalized expression of KCa3.1 in different subtypes of glioblastoma; n = 49 patients (mesenchymal), n = 31 patients (proneural), n = 26 patients (neural), and n = 39 patients (classical). **q**, Schematic illustration of main findings. Error bars show s.e.m. ns, not significant ($P \geq 0.05$).